Constraints on the Geometry and Frictional Properties of the Main Himalayan Thrust Using Coseismic, Postseismic, and Interseismic Deformation in Nepal

T. Ingleby[1] , T. J. Wright[1] , A. Hooper[1] , T. J. Craig[1] , and J. R. Elliott[1]

[1]COMET, School of Earth and Environment, University of Leeds, Leeds, UK

Abstract The geometry and frictional properties of a fault system are key parameters required to understand its seismic behavior. The Main Himalayan Thrust in Nepal is the type example of a continental megathrust and forms part of a fault system which accommodates a significant fraction of India-Eurasia convergence. Despite extensive study of this zone of shortening, the geometry of the fault system remains controversial. Here, we use interseismic, coseismic, and postseismic geodetic data in Nepal to investigate the proposed downdip geometries. We use interseismic and coseismic data from previous studies, acquired before and during the 2015 M_w 7.8 Gorkha earthquake. We then supplement these by processing our own postseismic deformation data, acquired following the Gorkha earthquake. We find that kinematic modeling of geodetic data alone cannot easily distinguish between the previously proposed geometries. We therefore develop a mechanical joint coseismic-postseismic slip inversion which simultaneously solves for the distribution of coseismic slip and rate-strengthening friction parameters. We run this inversion using the proposed geometries and find that they are all capable of explaining the majority of geodetic data. We find values for the rate parameter, a, from the rate-and-state friction law that are between 0.8 and 1.6×10^{-3}, depending on the geometry used. These values are in agreement with results from laboratory studies and those inferred from other earthquakes. We suggest that the limitations of earthquake cycle geodesy partly explain the continued controversy over the geometry and role of various faults in the Nepal Himalaya.

1. Introduction

Continental megathrusts are capable of hosting some of the largest earthquakes in the world (Hubbard et al., 2015). The size of dip-slip faulting earthquakes can be controlled by the downdip geometry of the fault system (e.g., Bonini et al., 2014; Elliott et al., 2011; Hubbard et al., 2016), and as such, the geometry of these fault systems is important for seismic hazard analysis. In addition to geometrical complexities playing a role in rupture size, regions with different frictional properties are also thought to be significant in controlling rupture propagation and arrest (e.g., Avouac et al., 2015; Jolivet et al., 2015; Perfettini et al., 2010).

The type example of a continental megathrust is the fault system underlying the Nepal Himalaya. India is currently converging with Eurasia at a rate of approximately 40 mm/yr, with roughly half of this convergence accommodated in the Himalaya on the southern border of the Tibetan Plateau (Stevens & Avouac, 2015). The way in which this convergence is accommodated remains controversial. In particular, the geometry of the system of faults over which shortening occurs is still debated (e.g., Hodges et al., 2004; Lavé & Avouac, 2001; Pandey et al., 1995; Wobus et al., 2005).

The M_w 7.8 Gorkha earthquake of 25 April 2015 has presented an opportunity to learn more about the causative fault system, with a large number of studies examining the rupture in detail. Unfortunately, a consensus has not yet emerged, and instead, the earthquake has highlighted the variety of possible geometries that can be inferred from a range of data sets. Geometries used to model coseismic slip include single planes (e.g., Avouac et al., 2015), faults incorporating a laterally continuous (e.g., Elliott et al., 2016) or spatially varying (e.g., Hubbard et al., 2016) midcrustal ramp, and models including a shallow splay fault (e.g., Whipple et al., 2016). Section 3 contains a more detailed explanation of the different proposed geometries.

Geodetic techniques such as Global Navigation Satellite Systems (GNSS), Interferometric Synthetic Aperture Radar (InSAR), and SAR/optical pixel tracking and leveling are powerful tools for investigating fault

geometry and slip at depth. Most of the works examining the Gorkha rupture have used geodesy to either infer the fault geometry (Elliott et al., 2016; Wang & Fialko, 2015; Whipple et al., 2016) or constrain the distribution of slip on an assumed geometry (Avouac et al., 2015; Galetzka et al., 2015; Grandin et al., 2015; Hubbard et al., 2016; Lindsey et al., 2015). Elliott et al. (2016) used interseismic deformation data as a further constraint in their investigation of possible fault geometries, although they solved for coseismic and interseismic geometries independently.

Here, we use geodetic data from each stage of the earthquake cycle in Nepal to test different downdip fault geometries. We seek time-invariant fault geometries that are capable of matching surface geodetic data satisfactorily, given estimates of their uncertainties. Coseismic and interseismic deformation data are readily available for Nepal, having been acquired prior to and during the 2015 M_w 7.8 Gorkha earthquake (e.g., Ader et al., 2012; Elliott et al., 2016; Galetzka et al., 2015; Jackson & Bilham, 1994; Lindsey et al., 2015). There have been a handful of postseismic deformation studies carried out for this event (Gualandi et al., 2016; Jiang et al., 2018; Mencin et al., 2016; Sreejith et al., 2016; Zhao et al., 2017). These postseismic studies find a relatively small deformation signal, which is more dependent on the data processing methods applied. We therefore independently process GNSS and InSAR data using approaches different from previous studies over Nepal to obtain our own postseismic deformation measurements, allowing for a comparison.

Deriving these postseismic deformation measurements also enables us to examine the continuing and evolving hazard following the Nepal earthquake. Palaeoseismology has shown that previous earthquakes have ruptured all the way to the surface, with many meters of slip along the Main Frontal Thrust (MFT) (Sapkota et al., 2013). However, the Gorkha earthquake failed to rupture to the surface, meaning a large section of the Main Himalayan Thrust (MHT) likely remains capable of producing future damaging earthquakes. Furthermore, the region to the west of the Gorkha earthquake remains an area of concern. The last large earthquake to occur here was in 1505 and could have exceeded M_w 8.5, leading to a potential slip deficit of over 10 m (Avouac et al., 2015; Bilham & Wallace, 2005). An alternative means of releasing strain on these portions of the MHT is through aseismic afterslip, which has been observed following a large number of earthquakes (Freed, 2007; Hearn, 2002; Ingleby & Wright, 2017; Wright et al., 2013). Determining which parts of the MHT are slipping aseismically is vital for assessing the ongoing seismic hazard in the region (Avouac et al., 2015).

Furthermore, any afterslip can be used to investigate the frictional properties of the sliding faults (e.g., Barbot & Fialko, 2010; Copley & Jolivet, 2016; Perfettini & Avouac, 2004; Wimpenny et al., 2017). Using the geometries constrained by earthquake cycle geodesy, we can obtain the stress transferred to other regions of the fault due to the earthquake. The relationship between the calculated stress change in these regions and the resulting inferred afterslip allows us to place constraints on frictional properties on the major faults in Nepal.

We begin by obtaining measurements of the postseismic deformation following the Gorkha event using GNSS and InSAR. Following this, we investigate possible fault geometries within Nepal in light of deformation data from various stages of the earthquake cycle. Finally, we use these geometries as a starting point for determining the frictional properties of the fault system by inverting for a self-consistent mechanical model of coseismic and postseismic slip.

2. Measurements of Postseismic Deformation

2.1. Previous Studies

There have been a number of postseismic deformation studies following the Gorkha event. Gualandi et al. (2016) used continuous GNSS stations in Nepal to study the transient postseismic deformation up until November 2015. They isolated the postseismic signal using independent component analysis and found that GNSS stations showed predominantly southward motion with the amount of motion increasing to a maximum of approximately 65 mm at CHLM. Mencin et al. (2016) also used GNSS stations to examine deformation following the Gorkha earthquake. They isolated the postseismic signal using a combination of interseismic and hydrological loading models and found a similar pattern of deformation to Gualandi et al. (2016). One problem faced by both of these studies is the lack of GNSS data on the Tibetan Plateau. This means that inferred postseismic deformation models are largely unconstrained north of the Himalayan range. Zhao et al. (2017) and Jiang et al. (2018) supplemented GNSS stations south of the Himalayan range with a small number of stations operating in southern Tibet. These far-field stations record small postseismic displacements toward the rupture zone, while the stations south of the range show similar displacements to other studies.

Sreejith et al. (2016) used InSAR, combined with four GNSS station time series, to examine postseismic deformation up to 88 days after the main shock. Their InSAR data provide further constraints to the north of the Himalayan range and supplement the GNSS data constraints. The InSAR results show a range decrease of 10–15 cm consistent with uplift north of the coseismic rupture. This is in broad agreement with GNSS stations showing increasing deformation to the north. Wang and Fialko (2018) present the most comprehensive range of postseismic deformation data to date, with GNSS data south of the Himalayan range up until March 2017 and InSAR data from several satellite tracks. Their results agree with the picture given by previous studies, and their InSAR data suggest relatively localized uplift north of the coseismic rupture.

Here, we use a combination of GNSS and InSAR data to measure the surface deformation following the Gorkha event. We use a Bayesian technique to estimate the GNSS postseismic position uncertainties and construct an InSAR time series using StaMPS (Hooper et al., 2012).

2.2. Data Sets
2.2.1. GNSS Data

We use GNSS stations which were deployed and maintained through a collaboration between California Institute of Technology and the Department of Mines and Geology (Nepal). Some additional stations were deployed by Roger Bilham, Rebecca Bendick, and David Mencin following the 2015 Gorkha earthquake. We use the 24-hr final daily position time series processed by the Nevada Geodetic Laboratory (http://geodesy. unr.edu/; last accessed on 23/8/2017) for all stations within the Nepal region. These daily solutions are processed using GIPSY/OASIS-ii Version 6.1.1 developed by JPL and are provided in the IGS08 reference frame. Full details of the processing are available online (http://geodesy.unr.edu/gps/ngl.acn.txt). We supplement the data available from the Nevada Geodetic Laboratory with some data provided by A. Gualandi, used in Gualandi et al. (2016).

The position time series obtained are the result of a number of signals which need to be accounted for in order to extract a transient, postseismic signal. These signals include a linear deformation rate, annual and semiannual loading, and offsets in the time series caused by equipment changes or earthquakes. In order to remove these signals, we fit a function to stations that had been recording for at least 1 year prior to the earthquake of the following form:

$$y(t)_{\text{preseismic}} = A + Bt + C\sin(2\pi t) + D\cos(2\pi t) + E\sin(4\pi t) + F\cos(4\pi t) + \mathcal{H}(t) \tag{1}$$

where A is a universal offset for the entire time series, Bt represents a linear rate, the sin and cos functions represent annual and semiannual signals, and $\mathcal{H}(t)$ is the Heaviside function, used to model offsets in the time series. If the offset times are known, then the equation becomes linear and can be solved using a linear least squares inversion. Offset times at each station were obtained from the potential step discontinuities database maintained at the Nevada Geodetic Laboratory (http://geodesy.unr.edu/NGLStationPages/steps. txt). Manual inspection of the time series confirmed that most of these step discontinuities were present. Extra offset times were added for stations MKLU, GRHI, XYAK, and BNDP at 0.57 years after the earthquake and at ODRE at 0.95 years after the earthquake. If there were many offset times within a short time span, we collapsed these to a single offset time to avoid overfitting the data.

We use a similar approach to previous studies (Gualandi et al., 2016; Wang & Fialko, 2018) and spatially interpolate the linear and seasonal fitting coefficients to those stations that were not recording for at least 1 year before the earthquake (see supporting information Figure S1 for details). Fitting coefficients are mostly consistent, but we exclude stations CTWN, NAST, and KIRT when performing the linear interpolation as their fitting coefficients appeared to be anomalously different from those of other stations around them. The resulting interpolated coefficients were used to remove signals not associated with postseismic deformation from the remaining GNSS sites. After this, GNSS time series show evidence of transient postseismic deformation, with the clearest signal visible at station CHLM (see Figure 1). The remaining time series should only contain transient postseismic deformation, but some sites show slight sinusoidal variations still. We therefore include some sinusoidal terms when extracting the postseismic signal in order to avoid fitting residual seasonal deformation as though it were postseismic.

$$y(t)_{\text{postseismic}} = \alpha \ln(1 + t/\tau) + \beta \sin(2\pi t) + \gamma \cos(2\pi t) + \mathcal{H}(t) + \delta \tag{2}$$

This equation includes a universal offset (δ), step discontinuities represented by the Heaviside function ($\mathcal{H}(t)$), seasonal terms (β and γ), and a logarithmic postseismic function. We use a Bayesian inversion technique to calculate a range of acceptable values for each of the unknowns. We use uniform prior probability

distributions for each parameter and use the data misfit as our likelihood function, assuming Gaussian errors on the data. Once the inversion has passed the "burn-in" stage, we keep a record of accepted models. We can then use these accepted models to predict displacements associated with each term in equation (2). In order to extract an estimate of postseismic deformation at any time after the earthquake, we predict displacements caused by all the terms in equation (2), except the logarithmic term. We do not use the displacement predicted by the logarithmic term to extract postseismic displacements at any time; instead, we subtract the predicted "nonpostseismic" displacements from the postseismic time series and then we extract all GNSS displacements within 6 days of the desired time. This is done for all accepted model fits to obtain a range of possible postseismic displacements, which we take the mean and standard deviation of. We estimate the displacement at each station at the time of each InSAR acquisition and after 1 and 2 years. This approach enables us to largely isolate the postseismic signal, without underestimating the error on that signal from both random noise and other sources of deformation. The resulting postseismic displacements after 1 and 2 years are shown in the maps in Figure 1. The map of postseismic displacements shows most deformation is concentrated near the coseismic rupture with very little deformation at large distances, where coseismic stress changes will be small. The fact that GNSS stations far from the coseismic rupture show little movement in our extracted postseismic displacements suggests our method is working as expected.

2.2.2. Postseismic InSAR

We use SAR images captured by the EU Copernicus satellite Sentinel-1a, operated by the European Space Agency (ESA). Sentinel-1a acquired images on both ascending and descending tracks covering the area of interest with a relatively short revisit time (12–36 days). Images were acquired in Interferometric Wide Swath mode with a footprint approximately 250 km wide and consist of a series of subimages known as bursts which we combined to form a larger mosaic. We formed small baseline interferograms with higher coherence using the Gamma software (http://www.gamma-rs.ch/), implemented within a modified version of LiCSAR (Wright et al., 2016) and prepared for input into a modified version of StaMPS for time series analysis (Hooper et al., 2012). We chose to use images from descending Track 19 up until 8 September 2015 and ascending Track 85 up until 23 November 2015. We ended our time series at these times due to a change in acquisition strategy causing a large time gap between these dates and the next data available on each track, thus reducing coherence. Furthermore, GNSS data from CHLM indicate that 43% of the displacement recorded after 2 years is accumulated by the end of 8 September 2015, even though this is only 18% of the 2 year observation period.

Initial inspection of the InSAR time series revealed very large signals (over 15 cm line of sight [LOS]) that were often correlated with topography. We suspected these signals were atmospheric signals and so investigated the effects of the atmosphere on InSAR signals in the area. We used the ERA-Interim (ERA-I) weather model reanalysis product (Bekaert, Walters, et al., 2015; Jolivet et al., 2011) and GNSS station estimates of atmospheric delay (Herring et al., 2013) to estimate the atmospheric signals present in the InSAR time series. Full details of our analysis can be found in the supporting information. The temporal variability of the atmosphere is highly changeable over the study area with much greater temporal variability in the Ganges basin compared to the Tibetan plateau, even after seasonal signals are removed.

We attempted to remove the atmospheric signal using both empirical approaches (Elliott et al., 2008) and weather model results (Bekaert, Walters, et al., 2015; Jolivet et al., 2011). Unfortunately, neither approach provided a satisfactory correction to our InSAR data (see Text S1 for more details). We therefore take a different approach and only use part of our InSAR data. GNSS stations and ERA-I nodes both show much lower temporal variability at greater heights (Figure S3). This is simply due to the fact that at higher elevations, the lower troposphere (where the largest delay variations occur) is thinner, thus introducing less opportunity to build up large variability (Bekaert, Hooper, et al., 2015). As well as the temporal variability, the atmosphere becomes more spatially variable over longer length scales and over large changes in topography. This suggests that analyzing a smaller region on one side of the large topographic change caused by the Himalayas would reduce the impact of large atmospheric variations. We therefore decided to only analyze InSAR data for heights over 4,000 m on the Tibetan plateau. We chose 4,000 m as a cutoff height as this provides a good balance between the number of available InSAR pixels and their atmospheric variability (see Figure S3d). Analyzing data from the plateau has a number of advantages, such as generally higher coherence, less atmospheric variation, and greater resolving power for the northward extent of postseismic deformation. While this approach means we discard large amounts of potentially useful data, we are less likely to misinterpret atmospheric or hydrological loading signals as tectonic ones. This approach also removes the risk of possible
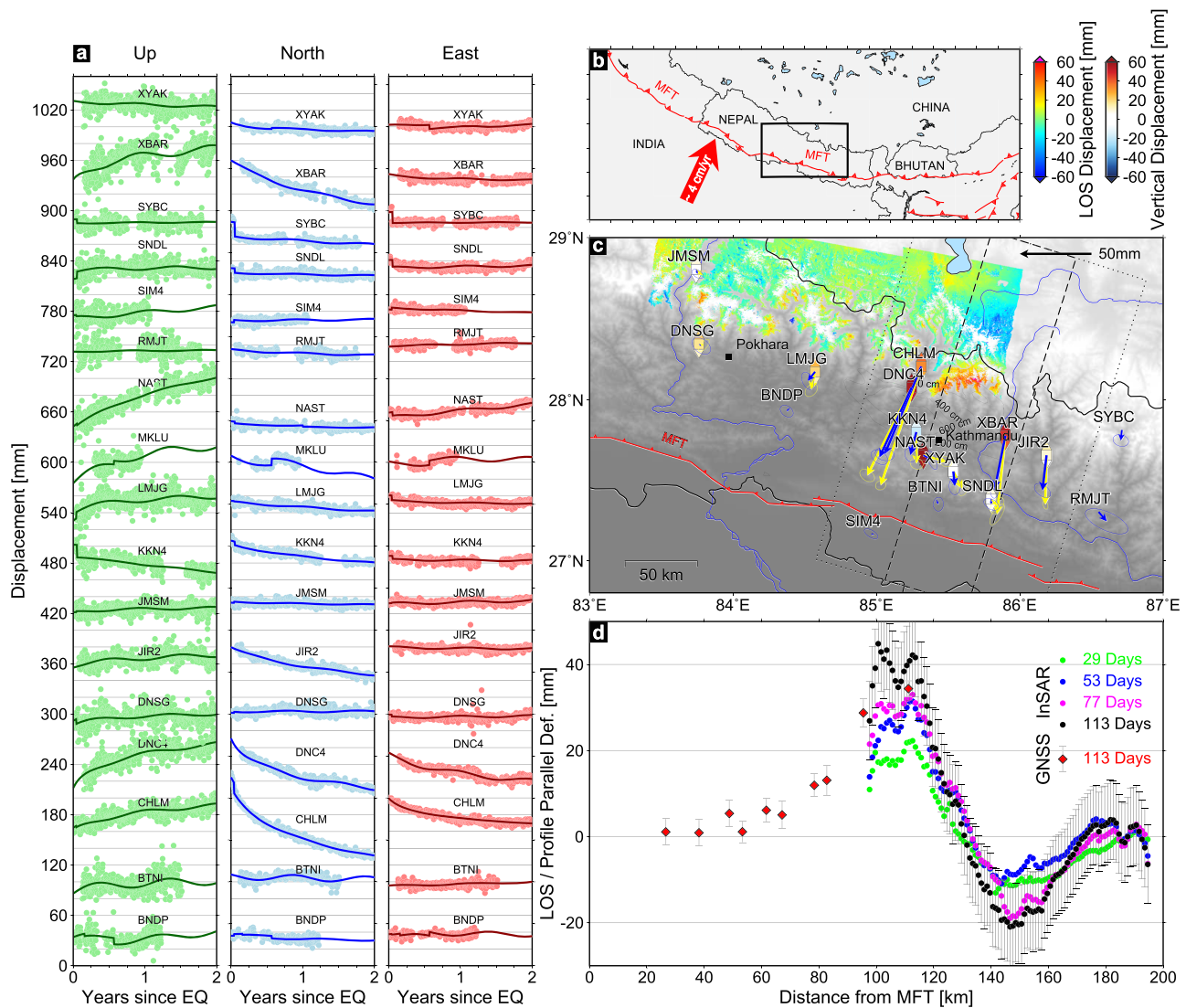
Figure 1. Postseismic deformation recorded by GNSS stations and InSAR. (a) Postseismic time series for each component at each station. Dots show the detrended postseismic position, and solid lines show the fit. (b) Location map. Red arrow shows Indian plate convergence. Black rectangle is area shown in panel c. (c) Map view of postseismic deformation showing GNSS displacements 1 year (blue) and 2 years (yellow) after the Gorkha earthquake. Color map shows line-of-sight (LOS) displacements from an interferogram spanning 29 April 2015 to 15 August 2015. Vertical GNSS displacements are shown as squares with triangles giving the 1-sigma range of values. Gray lines show coseismic slip contoured every 2 m from Elliott et al. (2016). Dashed and dotted boxes show the swath profiles used when sampling the InSAR and GNSS, respectively. (d) Profile through postseismic deformation. Red dots with error bars show profile-parallel GNSS. Colored and black dots show LOS deformation along the profile from different times after the earthquake. Black error bars show standard deviation of phase from an undeforming part of the Tibetan plateau for the 113 days interferogram. The earlier interferogram profiles have smaller error bars, but these are omitted for clarity. Larger version of panel (c) available in Figure S5 in the supporting information.

unwrapping errors over the Himalayas affecting our results. The resulting InSAR data are complementary to the GNSS data available at lower altitudes.

Initial analysis of the data shows a region of range decrease in the same location as found by Wang and Fialko (2018). In order to improve the signal-to-noise ratio of the plateau data, we apply a simple height based atmospheric correction:

$$\phi = ah + bx + cy + d \tag{3}$$

where h is the height, and x and y are InSAR pixel coordinates in kilometers. This correction simultaneously solves for a linear correlation between phase and topography and a bilinear ramp using only data from the plateau and excluding data in the deforming region. The inclusion of a bilinear ramp allows for the removal of any long wavelength atmospheric signals uncorrelated with topography. An example corrected

interferogram covering the period 29 April 2015 to 15 August 2015 is shown in Figure 1 as well as profiles through the InSAR time series. The interferograms which form the InSAR time series can be seen in Figure S4 in the supporting information.

2.3. Observations Summary

Some GNSS stations show a clear postseismic transient, indicating that postseismic deformation is taking place but is limited in its spatial extent (see Figure 1). The affected GNSS stations surround the coseismic rupture with stations to the north showing the greatest deformation (e.g., CHLM). These observations are in agreement with previously published work (Gualandi et al., 2016; Jiang et al., 2018; Mencin et al., 2016; Zhao et al., 2017).

Ascending and descending Sentinel-1a interferograms show significant surface deformation on the Tibetan plateau and provide a constraint on the northward extent of the postseismic deformation. They show that deformation is relatively localized and agree with the picture given by the GNSS stations alone. The InSAR deformation is clearest in the descending track (Track 019), with a lobe of motion toward the satellite just to the north of the coseismic rupture. This signal is similar to that seen by Sreejith et al. (2016) although smaller in extent, but is in good agreement with Wang and Fialko (2018). The ascending track (Track 085) also shows signals that may be caused by postseismic deformation, but these signals are not as consistent through time. We therefore choose to use only the descending data in our modeling. All data sets agree that deformation is primarily to the north of the center of coseismic deformation and is relatively focused (see Figure 1), in agreement with previous work.

2.4. Deformation Mechanism

Various postseismic deformation mechanisms may be responsible for the observed surface displacements (Ingleby & Wright, 2017). Distinguishing between afterslip and viscoelastic relaxation can be challenging (e.g., Hao et al., 2012; Perfettini & Avouac, 2004; Ryder et al., 2007; Savage, 1990; Wright et al., 2013). However, the combination of spatial and temporal modeling of surface displacements can be used to determine which deformation mechanism is primarily responsible (e.g., Freed, 2007, Freed et al., 2007; Jónsson et al., 2003).

The spatial location and extent of postseismic surface deformation for the Gorkha earthquake suggests that slip downdip of the coseismic rupture is a likely cause of the observations, as inferred by previous authors (Gualandi et al., 2016; Jiang et al., 2018; Mencin et al., 2016; Sreejith et al., 2016; Wang & Fialko, 2018; Zhao et al., 2017). We used VISCO-1D (Pollitz, 1997) to perform simple viscoelastic relaxation calculations. We tested a number of different viscosities and found that all models produce a much broader, lower amplitude surface deformation signal, with the opposite sense of motion to that seen in the data (see Figure S6 in the supporting information and accompanying details in Text S2 for further information). Previous work has found that limited viscoelastic relaxation is possible but is masked by the larger afterslip signal (Wang & Fialko, 2018). Zhao et al. (2017) suggest that some viscoelastic relaxation helps to explain far-field GNSS stations in southern Tibet and causes the spatial distribution of afterslip to have a more plausible extent. We therefore assume that the predominant cause of the near-field postseismic deformation we observe is afterslip. With this in mind, we use these postseismic deformation measurements in our investigation of the faults beneath Nepal.

3. Geometry of the Himalayan Fault System

3.1. Proposed Geometries

The 3-D geometry of the Himalayan fault system is still vigorously debated. The variety of geometries proposed fall in to three broad categories. These categories can be illustrated by summarizing the geometries used in slip inversions for the Gorkha earthquake (see Figure 2 for a cross section showing the geometries).

First, a number of authors have used a single, shallowly dipping fault plane to explain observations in the earthquake (e.g., Avouac et al., 2015; Galetzka et al., 2015; Grandin et al., 2015; Lindsey et al., 2015; Wang & Fialko, 2015). This simple model is able to explain most of the coseismic observations, as well as the largest aftershock and postseismic deformation observed using GNSS (Gualandi et al., 2016).

Second, some authors have used a flat-ramp-flat (FRF) geometry to model slip in the Gorkha event (e.g., Elliott et al., 2016; Hubbard et al., 2016; Sreejith et al., 2016). This geometry is also able to explain most of the observations and is generally chosen due to its ability to explain other aspects of the Himalayan orogeny such
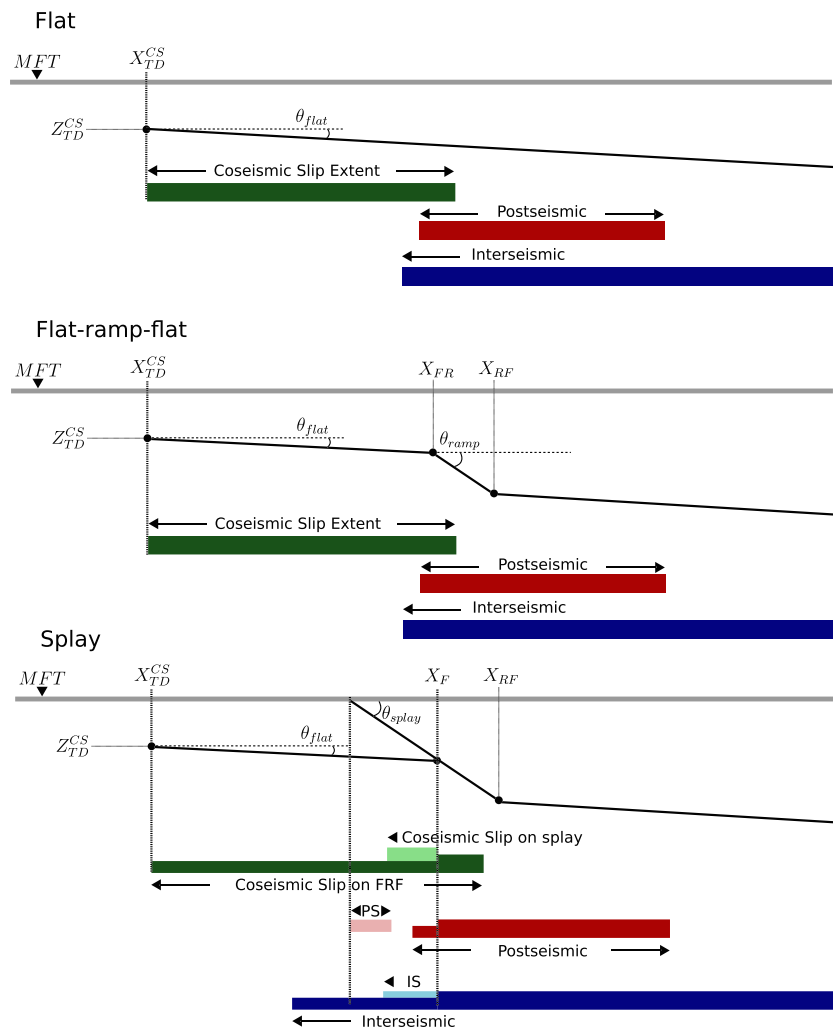
Figure 2. Diagram explaining the model setup with associated parameters. Top panel shows a parameterization of the single flat model. Middle panel shows the flat-ramp-flat geometry (similar to Elliott et al., 2016). Bottom panel shows a flat-ramp-flat geometry with a splay similar to Whipple et al. (2016). CS, PS, and IS refer to coseismic, postseismic, and interseismic slip on the splay, respectively. The thickness of the bars in the splay case show whether slip updip of the fault junction must equal slip downdip of the junction or not. TD refers to top depth and MFT is the Main Frontal Thrust surface trace.

as the location of microseismicity (Pandey et al., 1995), the location of a rapid change in uplift rates (Lavé & Avouac, 2001), and the geology (e.g., Hubbard et al., 2016). The complexity of these geometries varies from a single geometry along strike (Elliott et al., 2016; Sreejith et al., 2016) to full 3-D models with multiple ramps and along-strike variation (Hubbard et al., 2016; Qiu et al., 2016; Zhang et al., 2017). Laterally continuous FRF models have also been used to model postseismic deformation by Mencin et al. (2016) and Sreejith et al. (2016).

Third, Whipple et al. (2016) have used a single, shallowly dipping fault plane with a steeper splay fault to explain detailed aspects of the geodetic data in the Gorkha event. This model is also able to explain other aspects of the Himalayan orogeny since it advocates out-of-sequence thrusting as a mechanism for the rapid change in uplift rates and the building of topography (e.g., Hodges et al., 2004; Wobus et al., 2005).

3.2. Geometric Inversion Setup
3.2.1. Data
Here, we use geodetic data from all three stages of the earthquake cycle in Nepal to determine geometries that are capable of matching all three stages simultaneously. We use ALOS InSAR data from Lindsey et al. (2015) and Sentinel-1 InSAR data from Elliott et al. (2016), which record coseismic deformation. For the
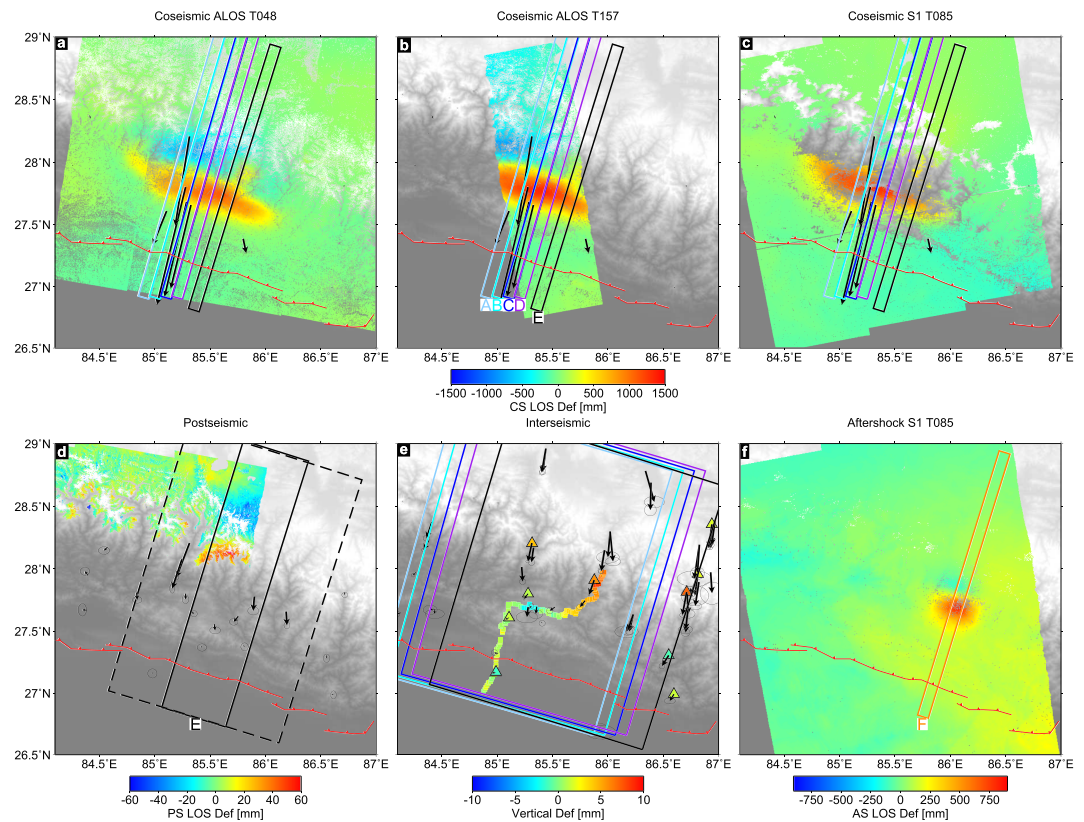
Figure 3. Summary of geodetic data used from each stage of the earthquake cycle. (a–c) Examples of coseismic data from ALOS (Lindsey et al., 2015) and Sentinel-1 (Elliott et al., 2016), as well as GNSS coseismic offsets as black arrows (Galetzka et al., 2015). Red sawtooth line is the surface trace of the Main Frontal Thrust (Taylor & Yin, 2009). Rectangles show swath profiles used in modeling labeled A–E in panel (b). (d) Postseismic interferogram from Sentinel-1 spanning 29 April 2015 to 15 August 2015 and GNSS displacements. Solid rectangle shows swath used for InSAR data. Dashed rectangle shows the wider swath used to obtain GNSS displacements. (e) Interseismic data: colored squares are vertical velocities obtained from leveling (Jackson & Bilham, 1994), colored triangles represent vertical GNSS velocities from Ader et al. (2012). Arrows are horizontal velocities from Kreemer et al. (2014). Rectangles are wider, interseismic swath profiles in the same locations as in (a). (f) Example of aftershock data from Sentinel-1. Orange rectangle labeled F is profile used in aftershock modeling.

postseismic period, we use the postseismic GNSS displacements accrued by 15 August 2015 and the interferogram covering the period 29 April 2015 to 15 August 2015. We use three data sets to capture the inerseismic deformation. First, we use horizontal GNSS velocities compiled for the Global Strain Rate Model by Kreemer et al. (2014). Unfortunately, vertical GNSS velocities are not available in this compilation, so instead we use vertical GNSS velocities from Ader et al. (2012), alongside leveling results obtained by Jackson and Bilham (1994). Figure 3 shows a summary of the data sets obtained as well as the location of profiles taken through each data set.

For several reasons, we choose to focus on profiles through the data. First, the interseismic leveling data (Jackson & Bilham, 1994) and GNSS data (Ader et al., 2012; Kreemer et al., 2014) are mostly in the form of orogen perpendicular profiles due to accessibility. Second, the downdip structure of the fault zone is primarily constrained by fault-perpendicular observations. Third, modeling individual profiles allows us to see if there is discernible variation along strike (Hubbard et al., 2016). Finally, modeling profiles is computationally faster, with fewer data points and model parameters. We use profiles taken perpendicular to the average strike of the surface trace of the MFT (287°), which are shown in Figure 3. These data are used in all our profile modeling, in both sections 3.3 and 3.4.

We use a number of profiles along strike to allow us to capture coseismic, postseismic, and interseismic deformation maxima as well as deformation due to the largest Gorkha aftershock (M_w7.1 on 12 May 2015). InSAR data along the profiles are averaged in successive bins to reduce the computational cost, while the

covariance matrix of each InSAR data set is constructed using an empirical variogram (e.g., Lohman & Simons, 2005; Oliver & Webster, 2014). Coseismic deformation is imaged by four interferograms, whereas we only use one postseismic interferogram when solving for the geometry. We therefore use a bin spacing of 2 km for the coseismic InSAR but only 1 km for the postseismic InSAR to increase the number of postseismic data available in our inversions. We project GNSS displacements (or interseismic GNSS velocities) into profile-parallel and profile-perpendicular components, with the profile-parallel component used in the modeling. We do not use the postseismic vertical GNSS data due to higher uncertainties on the results and less confidence that the postseismic deformation has been effectively isolated from other vertical signals. The swaths used for the postseismic and interseismic deformation are wider than the coseismic swath since there are fewer geodetic measurements available. The results of these projections can be seen in Figure 4. Data from overlapping or adjacent profiles will be influenced by similar slip extents at depth, blurring out any discernible short-lengthscale variation. We remove the subsidence signal seen in the interseismic leveling data near Kathmandu, which is likely due to water extraction (Jackson & Bilham, 1994). We also remove leveling data south of the MFT surface projection, because signals here are unlikely to be associated with motion on the main Himalayan fault system (Bettinelli et al., 2006; Grandin et al., 2012).

3.2.2. Method

Initially, in section 3.3, we find the single best uniform slip elastic dislocation (Okada, 1985) for each stage of the earthquake cycle independently. For the interseismic deformation, we consider a creeping dislocation which continues deep into Tibet (Elliott et al., 2016; Vergne et al., 2001). In all our models in sections 3.3 and 3.4, we use a Bayesian inversion scheme implemented using a Monte Carlo Markov chain method incorporating the Metropolis-Hastings algorithm (Mosegaard & Tarantola, 1995). Our inversion method begins by using simulated annealing to determine a high likelihood starting point for the Bayesian inversion (Bagnardi & Hooper, 2017). The step size is adjusted within the inversion if acceptance rates become too high or too low (Amey et al., 2018). Each elastic dislocation has five parameters in our profile-based, geometric inversions: distance from MFT to top of the dislocation, top depth, bottom depth, dip angle, and slip. We use uniform prior probability distributions for each parameter. Additional constraints on these parameters are introduced when using more complicated geometries in section 3.4.

In all our inversions, we assume a homogeneous elastic half space. Wang and Fialko (2018) showed that including topography and heterogeneous elastic properties can change surface displacement patterns by approximately 10%. Inversions including these effects suggested very similar fault slip patterns for a fixed fault geometry with differences of up to approximately 10% in slip magnitudes. However, we chose to use a homogeneous half space to enable more rapid calculation of the Greens functions for each new trial geometry. Wang and Fialko (2018) also found that the difference between models using homogeneous and heterogeneous elastic structures and/or topography is reduced for smoother slip distributions, indicating that other factors affect the inference of slip at depth. These other factors include different geometries, different layered velocity structures, and different degrees of smoothing. Our inversions account for the uncertainty in geometry and solve for the degree of smoothing where distributed slip is used (sections 3.4 and 4). However, we do not account for any other uncertainties in the forward model, such as errors in elastic structure (Duputel et al., 2014; Ragon et al., 2018) or those introduced by failing to account for topography (Ben Thompson & Meade, 2018; Wang & Fialko, 2018). Inclusion of such model errors would increase the final uncertainties in our results.

We keep a record of each accepted model, providing us with probability distribution functions (PDF) for each model parameter. We combine the various geometric parameter PDFs (dips, depths, and distances) to construct a picture of likely fault models at depth. We determine where a fault model intersects a grid of 1×1 km squares beneath Nepal and produce a grid showing the possible geometries. Within these grids, darker colors correspond to a higher density of possible fault models in any given cell (see Figure 5).

3.3. Independent Coseismic, Postseismic, and Interseismic Inversions
3.3.1. Single Dislocations

Figure 4 shows the results of our inversions for each stage of the earthquake cycle independently. The majority of the surface deformation data can be explained using shallowly dipping elastic dislocations. Coseismic data from western profiles (A and B) are best fit using a dislocation dipping at 9.5–10.5°. Interseismic geodetic observations from throughout Nepal are best fit by a creeping interseismic dislocation which extends from near the lower-edge of the coseismic rupture with a similar dip (8–14°). Postseismic data from profile E are
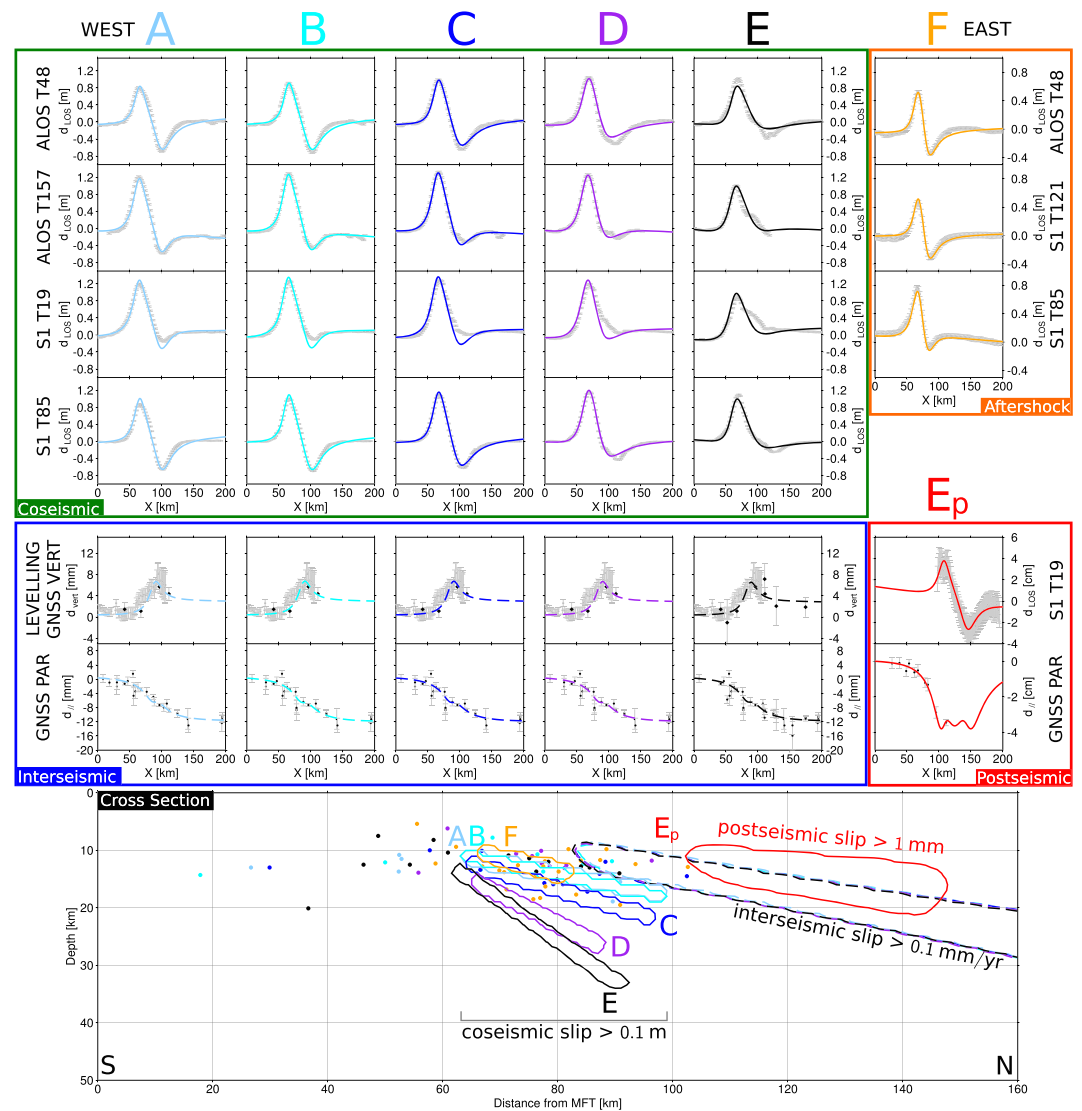
Figure 4. Profile data and model results from the independent inversions for each earthquake cycle stage. Letters correspond to profile labels in Figure 3. Far right panels show aftershock profile data and postseismic data. Colored lines show the model fit with the corresponding location of causative slip shown in the same color as a polygon on the cross section below. The colored polygons outline areas with an average slip higher than that labeled. Colored dots are aftershocks from Bai et al. (2016), color coded according to which profile they fall in.

best fit by a shallowly dipping fault with a similar geometry to that suggested by interseismic deformation. Furthermore, data from the M_w 7.1 aftershock (profile F) also suggest a fault with a similar geometry.

Combining the results of all these geodetic inversions, we see that most of the deformation is best fit by slip on a shallowly dipping (10°) fault. The most significant deviation from this geometry (best fit dip of 35°) is suggested by coseismic data from profile E that passes through the uplift anomaly identified by Whipple et al. (2016). This change in dip may be real and highlight a variable geometry along strike, as has been suggested by previous authors (e.g., Hubbard et al., 2016; Zhang et al., 2017). Alternatively, rather than the dip of a single, planar MHT changing along strike, a more complicated downdip geometry may be able to explain the data from profile E. We therefore try a series of more complex geometries to model data from profile E in subsequent sections. These more complex geometries are not precluded by our analysis so far, and may be hinted at by the higher density of aftershocks in the east (Adhikari et al., 2015; Bai et al., 2016).

3.3.2. Predefined Geometries

We first test the exact downdip geometries proposed by Elliott et al. (2016), Whipple et al. (2016) and Hubbard et al. (2016) by solving for distributed slip on each fixed geometry. We construct the geometries
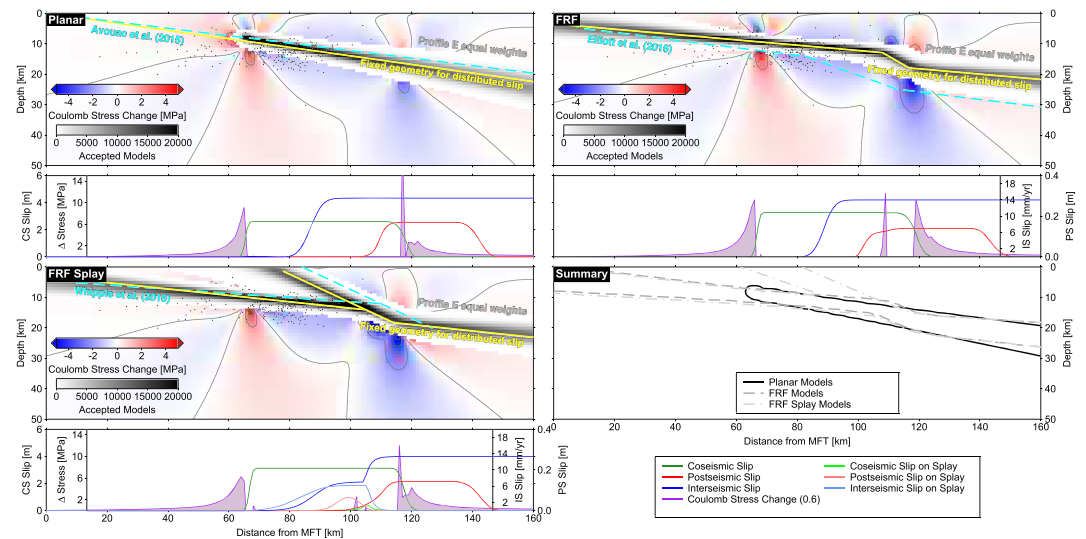
Figure 5. Summary of different inferred geometries. For each geometry, the top panel shows a cross section beneath Nepal, and the lower panel shows slip and stress changes on the inferred faults. The cross section shows the range of possible geometries obtained using the inversion with equal weight given to each earthquake cycle stage as a grayscale grid. The yellow lines correspond to the geometry used for distributed slip modeling in subsequent sections. Cyan lines are similar geometries from other studies. Slip in each stage of the earthquake cycle is shown by the mean in the lower panels, colored as indicated in the legend. The summary figure shows the region with >1,000 accepted models for each geometry.

based on the geometric parameters provided in Elliott et al. (2016) and Whipple et al. (2016) and take a profile through the geometry of Hubbard et al. (2016). We split the downdip geometries into 5 km square fault patches and solve for the amount of slip on each patch in each stage of the earthquake cycle. Since the geometry is fixed, each earthquake cycle stage can be modeled independently. We use a Bayesian inversion and apply smoothing to each stage of the earthquake cycle separately by using a Laplacian operator and solving for the degree of smoothing in the inversion (Fukuda & Johnson, 2008). The resulting slip on each of the profiles is shown in Figure S7. We found that all three geometries gave similar total variance reductions (VRs) (see Figures S8 and S9 in the supporting information). Each of the geometries could fit the coseismic data reasonably well, although the geometries proposed by Elliott et al. (2016) and Hubbard et al. (2016) gave slightly higher VR values (Figure S9). However, the geometries of Elliott et al. (2016) and Hubbard et al. (2016) could not reproduce the postseismic deformation particularly well (Figures S8 and S9), particularly the wavelength of the signal, which is approximately 80 km. This is likely due to their proposed geometries being relatively deep in the location where postseismic slip is required.

3.4. Joint Coseismic, Postseismic, and Interseismic Inversions

We now move on to using coseismic, interseismic, and postseismic data together to invert for satisfactory geometries to fit all geodetic data from profile E. We focus on testing the three classes of geometric model discussed in section 3: planar models, midcrustal ramp models, and splay models.

We therefore solve for our own version of each type of geometry, allowing the positions of ramps and splays to vary. We use the coseismic, interseismic, and postseismic data from profile E, as shown in Figures 3 and 4, in a joint inversion for the optimal model geometries. We then test whether slip on faults with these geometries can explain coseismic and interseismic data from the profile A. We perform the joint inversions in a Bayesian sense, where the likelihood of each model is calculated using the fits to the coseismic, postseismic, and interseismic data. We use the same inversion procedure as described in section 3.2 with uniform priors for each parameter. The bounds of these priors, as well as any other constraints, are explained in the appropriate subsequent sections. We again produce a grid of the possible geometries in cross section, as described in section 3.2 and show the range of slip values in each earthquake cycle stage at different distances along the profile (see Figure 5).

We consider there to be two end-member approaches when determining the likelihood of a proposed geometry. The first approach uses the data errors alone as weights in the inversion (as done in section 3.3). In this

case, the fit to the coseismic data ends up dominating the inversion as there are more coseismic data and the signal-to-noise ratio is much higher. A second approach uses the data errors and additional weighting factors to balance the contributions from different earthquake cycle data sets. This approach is necessary to account for incorrect model assumptions favoring a fit to one data set at the expense of all others. These weighting factors are implemented by scaling the coseismic and interseismic data variance-covariance matrices with respect to the postseismic data variance-covariance matrix. This maintains the relative errors between the data sets (e.g., InSAR and GNSS) in each stage of the earthquake cycle but alters the relative weighting between stages of the earthquake cycle (e.g., coseismic and postseismic). We determined the relative weights by calculating the weighted residual for a 1% error on all data from each stage of the earthquake cycle. For example, the weighted residual for the coseismic data is calculated as

$$R_{cs} = (\mathbf{d_{cs}} - 0.99\mathbf{d_{cs}})^\top \mathbf{C_{cs}^{-1}} (\mathbf{d_{cs}} - 0.99\mathbf{d_{cs}}) \tag{4}$$

where d_{cs} is the coseismic data vector and C_{cs}^{-1} is the inverse of the coseismic variance-covariance matrix. This is repeated for the postseismic and interseismic data. We then divide the postseismic residuals by the coseismic and interseismic residuals and use these ratios as weights such that $w_{ps} = 1$, $w_{cs} = R_{ps}/R_{cs}(= 0.0095)$, and $w_{is} = R_{ps}/R_{is}(= 0.1557)$.

We tested both approaches in our inversions and compared the results for the different geometries. We found that downweighting the coseismic and interseismic data had little effect on the overall quality of the fit to these data. In contrast, there was a noticeable improvement in the fit to the postseismic data when they played a greater role in the inversion. Artificially increasing the errors on the coseismic and interseismic data allowed a greater spread of acceptable models. While this greater range of acceptable geometries is due to our artificial increase of the coseismic and interseismic data errors, we suggest that a larger range of acceptable models is preferable given that we have not formally considered model errors in the inversion. We found that the inversion using data errors alone gave an optimal geometry that was different from that obtained using the weighted inversion, although they generally agreed within error. We therefore proceed using the results of our inversions with approximately equal weights for each stage of the earthquake cycle. Results of inversions using data weights alone can be found in the supporting information.

3.4.1. Planar Geometry
We first tried solving for the best fit single planar geometry using the coseismic, postseismic, and interseismic data from profile E, as used in previous inversions. The range of acceptable geometries from this inversion are shown in Figure 5 as a grayscale grid with darker shades representing the most likely geometry. The range of acceptable geometries is similar to the majority of best fitting faults in section 3.3. The corresponding data fits are shown in Figure 6. The range of acceptable models overlaps with the best fit models inferred using the data errors alone and agrees with the geometry used by Avouac et al. (2015).

Uniform slip can explain most of the data well, but struggles to explain eastern coseismic data from profile E. We therefore split the geometry into a series of smaller fault patches, solving for distributed slip in a Bayesian sense for each stage of the earthquake cycle. Creating a discretized fault plane limits our ability to exactly reproduce the maximum likelihood geometry suggested by uniform slip. Instead, we use a geometry which is similar to the mean geometry suggested by our uniform slip inversions. The fixed geometry dips at 8° from the surface trace of the MFT and is split into 40 patches with downdip width of 5 km and is shown in Figure 5. Since the geometry is fixed, we model each earthquake cycle stage independently. We model data from both east and west Nepal (profiles E and A, respectively) to check whether models obtained using the eastern Nepal data are still capable of matching the western Nepal data. Full details of all our distributed slip inversions can be found in the supporting information (see Text S3 and Figures S10–S16). We find that distributed slip models made only minimal improvements in the fit to the data (see Figures S11 and S16). In some cases, the VR provided by distributed slip is worse than that given by uniform slip. This is likely due to the fixed geometry we choose not necessarily matching the maximum likelihood geometry suggested by uniform slip. Furthermore, a slightly worse fit may be caused by the edges of the discretized fault patch boundaries not aligning with the edges of the uniform slip dislocations and the addition of smoothing.

3.4.2. FRF Geometry
Next, we try a system involving three faults connected downdip, illustrated in the middle panel of Figure 2. The top and bottom faults are given the same, shallow dip (between 2° and 15°) while the middle fault can have a different dip, which is allowed to reach steeper dip angles (2° to 30°). The positions and extents of each of the faults are solved for in the inversion with the constraint that the faults are joined downdip.
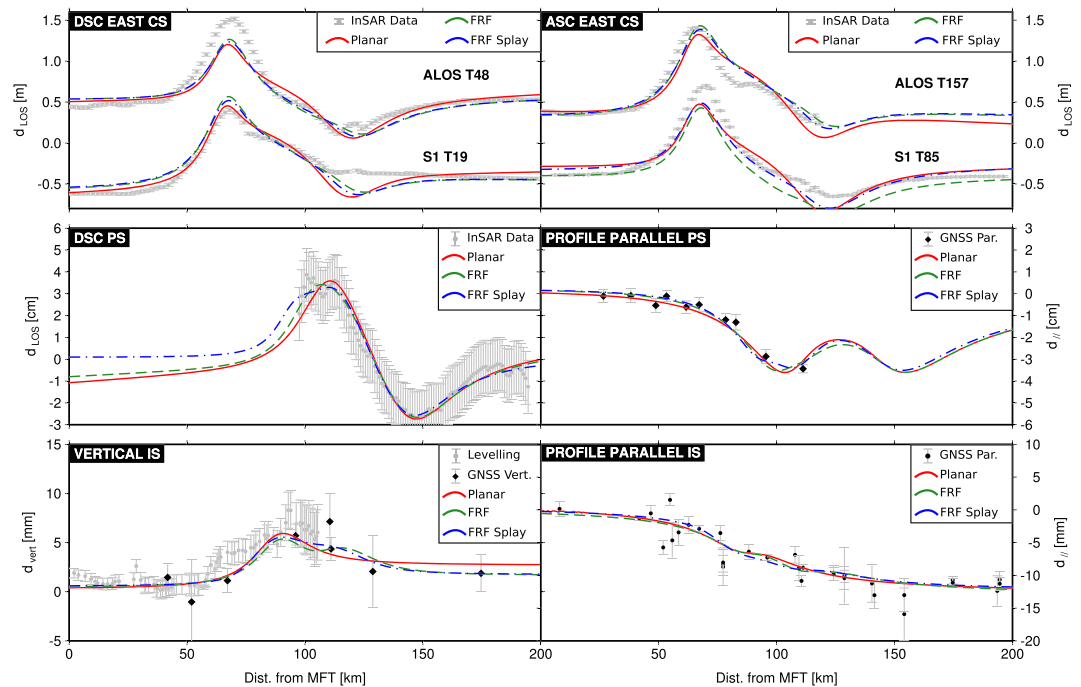
Figure 6. Summary of model fits to coseismic (CS), postseismic (PS), and interseismic (IS) data profiles. All three geometric models produce very similar fits to all data sets.

This means these three faults are capable of producing geometries ranging from a single, planar geometry through to a FRF geometry. We use data from the eastern profile (profile E) to solve for the optimal geometry. The geometry of the fault system as well as the extent and magnitude of slip in each earthquake cycle stage is varied in each trial.

Figures 5 and 6 show the range of acceptable models and the fit to the data. The addition of a midcrustal ramp enables a better fit to the coseismic data using uniform slip but has minimal effect on the fit to the interseismic and postseismic data. Our range of acceptable models places the midcrustal ramp 20–30 km further north than the model proposed by Elliott et al. (2016). This discrepancy can be explained by our inclusion of postseismic data when resolving the best fit geometry and the range of acceptable models suggested by Elliott et al. (2016) (e.g., see Figure 3 of Elliott et al., 2016). When coseismic data contribute more to our inversion, the best fit ramp moves further south but with little visible improvement in fit to the data. We then fix the geometry as shown in Figure 5 and split this into a number of patches. We solve for distributed slip in each stage of the earthquake cycle independently, in both the east and west as discussed above. We find that the distributed slip model is capable of fitting both eastern and western data but that the improvement in overall fit is even smaller than the planar case (see Figures S13 and S16).

3.4.3. FRF Splay Geometry

Finally, we try a FRF geometry with the ramp extending toward the surface as a splay, illustrated in the lower panel of Figure 2. This model resembles that used in Whipple et al. (2016) and allows for out-of-sequence thrusting in the earthquake cycle. The FRF geometric parameters are similar to the FRF model, but the parameter ranges are restricted to be similar to the model of Whipple et al. (2016). The locations and extents of each fault are solved for in the inversion, with the constraint that the whole fault system is connected downdip. The splay has the same dip as the ramp and can reach up to the surface. The slip on the splay is solved for as a fraction of the slip on the main FRF fault for each earthquake cycle stage. Coseismic slip on the splay is forced to have a bottom depth at the base of the splay but can have a top depth anywhere up to the surface. Postseismic slip can be anywhere on the splay with no constraints. Interseismic slip on the splay extends from the base of the splay up. Furthermore, the total interseismic slip rate on the splay and updip of the junction on the main FRF fault must be less than or equal to the slip rate below the junction.

We once again combine all deformation data together and solve for a consistent geometry. Results of these inversions are shown in Figures 5 and 6. The inferred geometry is similar to that suggested by Whipple et al.

(2016) but the most likely location of the ramp/splay is approximately 10 km further south, similar to our FRF geometry. Coseismic and postseismic slip on the splay is minimal, but the inversion places interseismic slip on the splay to give a sharper change in uplift rates. We then split this geometry into a number of patches downdip and solve for slip as in previous examples. More patches are required to construct this geometry due to the splay fault. As before, since the geometry is fixed, we can solve for slip in each stage of the earthquake cycle independently. The distributed slip inversion again provides only a minor improvement in fit (see Figures S15 and S16).

3.5. Assessing the Geometries

We have now tested the three main candidate geometries against geodetic data from throughout the earthquake cycle. We compare the fits of each model quantitatively using the weighted percentage VR achieved by each model (e.g., Huang et al., 2016), defined as

$$VR = \left[1 - \frac{(\mathbf{d} - \hat{\mathbf{d}})^\top \mathbf{C}^{-1}(\mathbf{d} - \hat{\mathbf{d}})}{\mathbf{d}^\top \mathbf{C}^{-1}\mathbf{d}} \right] \times 100 \tag{5}$$

where d is the data vector, $\hat{d}$ is the data predicted by the model, and C^{-1} is the inverse of the variance-covariance matrix. We calculate the VR for our two inversion weighting schemes and compare the results. All three geometries are capable of high total VR (> 90%), and the difference between them is minimal; however, the inversion is weighted (see Figure S16). Our kinematic slip inversion results offer no clear best candidate geometry. This goes some way to explaining why the geometry of the Himalayan thrust system remains controversial: different model geometries are capable of producing similar fits to surface deformation data.

An alternative approach to determine the best geometry is to test the physical consistency of each model. One way of doing this is to use the relationship between coseismic slip and postseismic afterslip. Afterslip is a function of the coseismic stress change (determined by coseismic slip), fault geometry and frictional properties (e.g., Barbot et al., 2009; Feng et al., 2016; Rousset et al., 2012). We can therefore use a stress transfer based model of afterslip to test the proposed geometries. We next use geodetic data and mechanical afterslip models to attempt to distinguish between the proposed geometries and infer the frictional properties of the faults beneath Nepal.

4. Frictional Properties of the MHT

4.1. Method

Many previous studies have used postseismic deformation as a means of determining the frictional properties of faults (e.g., Barbot et al., 2009; Chang et al., 2013; Hearn, 2002; Hussain et al., 2016; Perfettini & Avouac, 2004; Thomas et al., 2017). Most of these studies assume a rate-and-state friction law (Marone, 1998) where fault friction is related to sliding rate and the state of the fault (e.g., contact time). Often, the law is simplified using a rate-strengthening approximation when modeling afterslip (e.g., Barbot et al., 2009; Chang et al., 2013; Feng et al., 2016; Perfettini & Avouac, 2004). The complexity of the rate-strengthening model used varies. The simplest models solve for uniform frictional properties for a fault using the time dependence of a single GNSS station (Perfettini & Avouac, 2004). More complex models use the spatial and temporal variation of displacements to solve for uniform frictional properties on the fault (Feng et al., 2016; Wimpenny et al., 2017). The most complex models solve for spatially variable frictional properties over the fault (Barbot et al., 2009; Chang et al., 2013).

In all these cases, postseismic afterslip is driven by the coseismic stress change caused by the earthquake. This stress change is obtained using the coseismic slip distribution (Barbot et al., 2009; Chang et al., 2013; Feng et al., 2016; Wimpenny et al., 2017) or an estimate of the average stress change caused by the earthquake in the region slipping postseismically (Perfettini & Avouac, 2004). In all these cases, the coseismic stress change is assumed as a known term. However, this stress change strongly depends on the earthquake slip distribution, which is not perfectly known. Some studies take account of this uncertainty by collapsing the coseismic slip distribution to a smaller region and rescaling the slip to maintain seismic moment (Barbot et al., 2009; Wimpenny et al., 2017). Others use a variety of slip distributions from different authors to investigate the effects of these differences (Chang et al., 2013).

Here, we take account of the uncertainty in the coseismic slip distribution explicitly by jointly solving for both coseismic slip and the frictional properties of the fault. We smooth the coseismic slip using a Laplacian operator but also solve for the degree of smoothing in the inversion as a hyperparameter (Fukuda &

Johnson, 2008). This means that while the stress changes caused by coseismic slip are affected by the degree of smoothing, we let the inversion decide the best balance between smooth slip and the fit to the coseismic and postseismic data. Joint coseismic and postseismic slip inversions have been performed before (e.g., Wang et al., 2012) but without a mechanical link between the coseismic slip and postseismic slip. We use a generalized version of the rate-strengthening friction law to link coseismic slip and postseismic slip via the coseismic stress change and frictional parameters, assuming steady state (Barbot et al., 2009; Feng et al., 2016; Rousset et al., 2012):

$$V(t) = 2V_0 \sinh \frac{\Delta\tau(t)}{a\sigma} \tag{6}$$

This model provides fault sliding velocities, V, at a time, t, after an earthquake. Velocities are multiplied by a specified time step to give the displacement accrued over a short time interval. These displacements are then used to recalculate the total driving stress. V_0 is a reference slip rate (not equivalent to the interseismic slip rate) that controls the timescale of afterslip evolution—larger values of V_0 give larger stress-driven displacements in a specified time step, leading to faster stress relaxation. a is the rate dependence of friction from the rate-and-state friction laws, and σ is the normal stress. The steady state assumption is true when the total slip is much greater than the critical slip distance, D_c. In our inversions, cumulative postseismic slip is on the order of 10^{-2}–10^{-1} m, whereas laboratory-derived values for D_c are on the order of 10^{-5} m (Scholz, 1988), that is, total slip $\gg D_c$. $\Delta\tau(t)$ is the total shear stress change at time t after the earthquake, which we calculate as

$$\Delta\tau(t) = \Delta\tau_{\mathrm{coseismic}} + \Delta\tau_{\mathrm{aftershock}} + \Delta\tau_{\mathrm{afterslip}}(t) \tag{7}$$

This shear stress change is made up of a shear stress change from the earthquake, a shear stress change from the largest aftershock and ongoing shear stress changes from the evolving afterslip. We calculate the incremental displacements using a Runge-Kutta method with adaptive time steps with a maximum error of 1 mm at any time step. The incremental shear stress change caused by the incremental afterslip is added to the current total stress and used to drive further afterslip. This allows for the spreading out of postseismic deformation through time and allows postseismic slip to migrate into areas which may have slipped coseismically.

We assume the fault is entirely rate strengthening and solve for positive values of a. We acknowledge that parts of the fault must be rate weakening in order for earthquakes to nucleate. With a rate-strengthening only friction law, patches with little or no postseismic slip can be produced by giving those patches very low values of V_0 and/or high values of a (see equation 6). These patches are likely rate weakening and locked. σ is the normal stress at each patch, which is assumed to be lithostatic using an average rock density of 2,670 kg m^{-3}. As in Feng et al. (2016), we assume that the normal stress change is small (≈ 0.1 MPa) compared to the total normal stress (≈ 350 MPa) and therefore that the Coulomb stress change can be well approximated by the shear stress change alone.

All our kinematic slip inversions suggest that postseismic slip is restricted to areas downdip of the coseismic rupture. However, shear stresses are increased both downdip and updip of the earthquake, which would produce afterslip updip of the rupture as well on a fault with uniform rate-strengthening properties. Previous studies using stress-driven afterslip models for the Gorkha earthquake have had to only allow postseismic slip downdip of the rupture (Wang & Fialko, 2018; Zhao et al., 2017). We account for this need to have different amounts of slip updip and downdip of the rupture by solving for depth-dependent frictional properties. In the very shallow crust (depth <5 km), we set a to be very high in order to prevent postseismic slip and numerical instability caused by low lithostatic normal stresses. Below these depths, we solve for a single value of a, but we incorporate a depth dependence in V_0. We are not necessarily suggesting that there is any significant variation with depth in V_0, rather we use this depth dependence to solve for a smooth transition from locked to sliding at an unknown depth. This enables the transition from negligible afterslip (low values of V_0) to significant afterslip (higher values of V_0) to be determined in the inversion rather than imposed a priori, thus enabling uncertainties to be fully propagated. We use a logistic function to parameterize the depth dependence as a sigmoid:

$$V_0(z) = \frac{V_0}{1 + \exp(-k(z - z_0))} \tag{8}$$
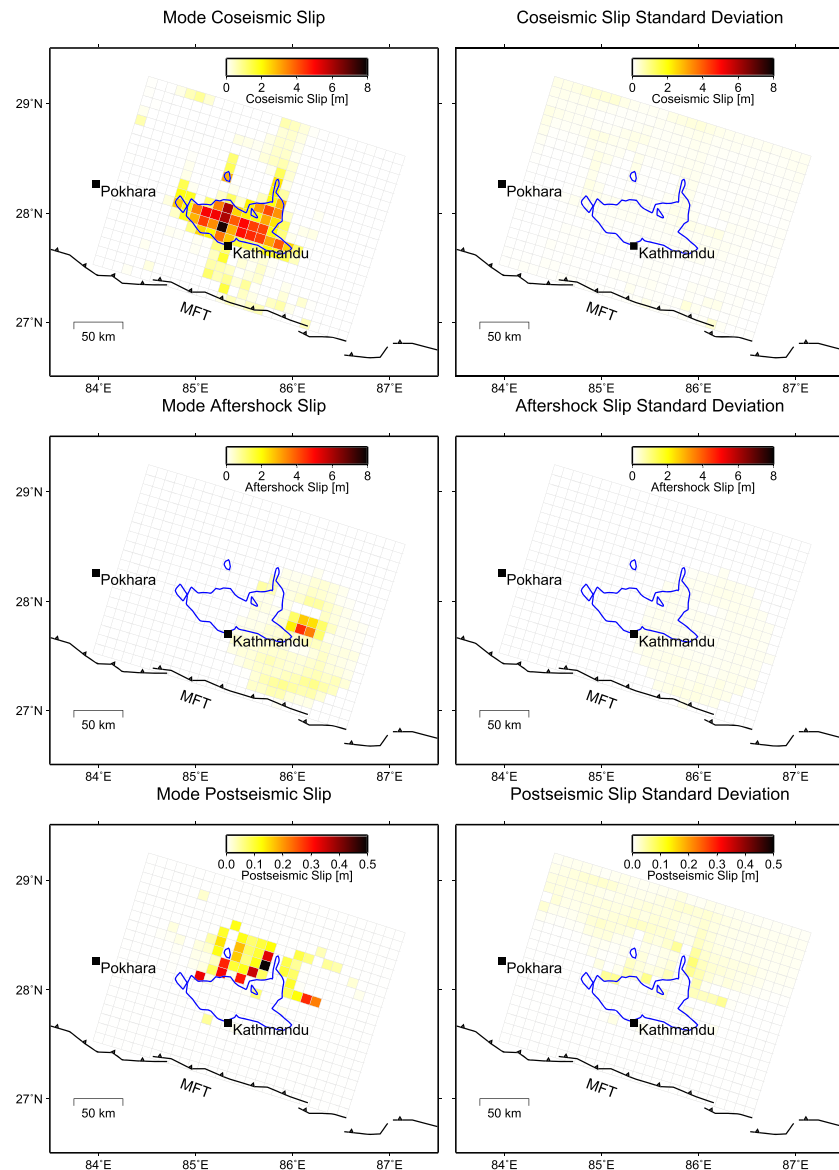
Figure 7. Results for the frictional afterslip model on the single planar geometry. Data used to obtain these results are described in section 4. Note that the color bar is different for coseismic and postseismic slips. Blue line shows the 2 m contour of mean coseismic slip. (top row) Mode and standard deviation of coseismic slip. (middle row) Mode and standard deviation of aftershock slip. (bottom row) Mode and standard deviation of postseismic slip on 8 September 2015.

We solve for the midpoint (z_0) and the steepness (k) of the sigmoid in the inversion. We used a smooth function to define the depth dependence to aid the inversion. We found that functions with a sharp transition depth caused problems in inversions with discrete downdip patches. Solving for the parameters z_0 and k allows for a range of depth-dependent V_0 curves. We allow V_0 to reach values up to 0.1 m/yr as previous work has found V_0 to be on the order of the interseismic loading rate (Barbot et al., 2009; Wimpenny et al., 2017). Given the lack of shallow afterslip in kinematic inversions, we set a to be very high for patches at depths shallower than 5 km to prevent postseismic slip and numerical instability in these patches with low lithostatic normal stresses.

Our novel approach enables us to use coseismic and postseismic observations together in the inversion, therefore allowing uncertainties in coseismic slip to propagate into uncertainties in our afterslip parameters. We use four coseismic interferograms (ALOS T48 and T157 Lindsey et al., 2015 and Sentinel-1 T85 and T19 Elliott et al., 2016), downsampled using a quadtree approach (Decriem et al., 2010). We also include
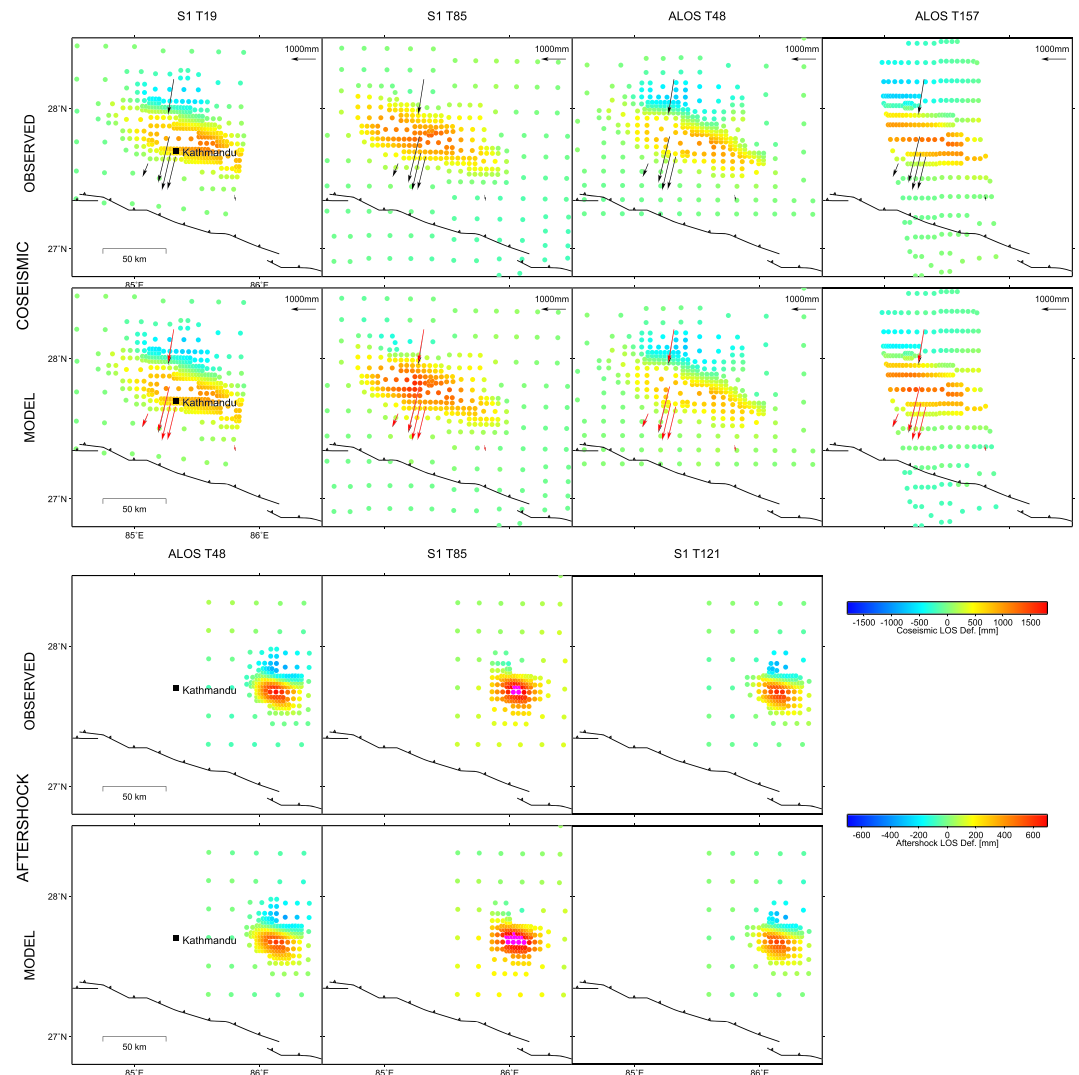
Figure 8. Coseismic and aftershock displacements for the single planar geometry. (first and second rows) The InSAR and GNSS displacements from the main shock as well as the mean model fit. Note that red, predicted GNSS arrows overlie black, observed arrows in the model displacements. (third and fourth rows) The InSAR displacements from the aftershock and corresponding mean model fit.

coseismic GNSS offsets from Galetzka et al. (2015) in the inversion, and solve for slip in the largest aftershock (M_w7.1 on 12 May 2015) using ALOS T48 and Sentinel-1 T85 and T121 interferograms. We use the Sentinel-1 T19 postseismic deformation time series obtained in this study with all displacements relative to the first date (29 April 2015). The lower signal-to-noise ratio of these data made a quadtree based downsampling approach impractical since noise was often also highlighted by this gradient based approach. Instead we use a downsampling scheme with more sampling near the region of postseismic deformation. As in section 3.2, we do not use the vertical GNSS data in our modeling. Horiztonal postseismic GNSS displacements are extracted at each of the InSAR epochs using the method described in section 2.2.1. We recognize that this means our model may not perfectly capture any rapid postseismic deformation that occurs in the 4 days between the earthquake and the first SAR postseismic acquisition. While our models calculate displacements using a daily time step, we only compare with postseismic data (GNSS and InSAR) at the InSAR acquisition times.

We use the fault geometries obtained in our earlier kinematic inversions as the input for the joint coseismic-postseismic slip inversion. These geometries are extended along strike and then split into multiple square patches with length 10 km. We use the formulations of Okada (1985, 1992) to calculate the necessary elastic kernels used for both the expected stress and surface displacements from slip of 1 m on a fault
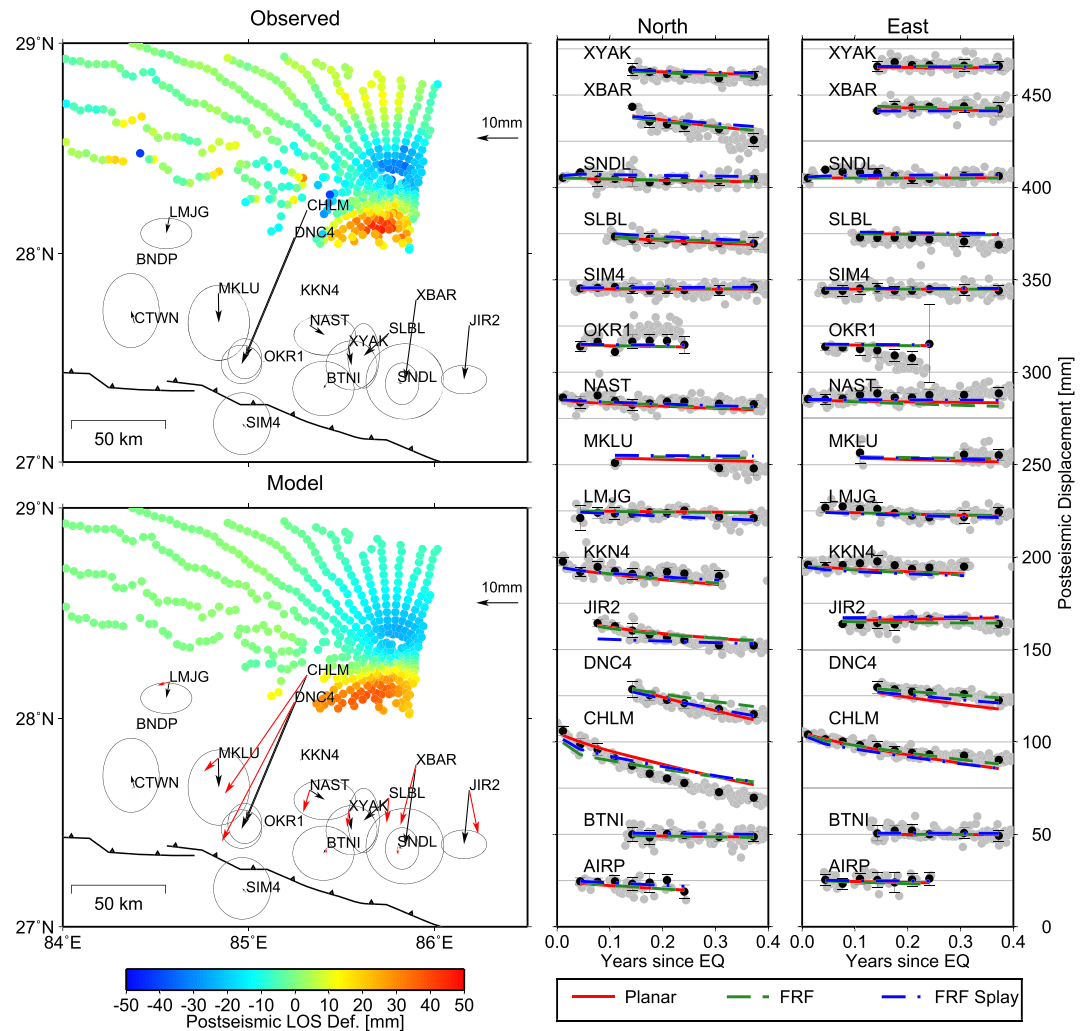
Figure 9. Postseismic displacements from stress-driven afterslip model. (top left panel) The final postseismic InSAR and GNSS displacements (8 September 2015). (bottom left panel) The InSAR and GNSS (red arrows) displacements at the same date predicted by the mean model for the single planar geometry. (right column) The GNSS time series for stations close to the coseismic rupture, with data points used in the inversion as black error bars and the different model fits as colored lines. Note that no vertical GNSS displacements were used in the inversion.

patch. We first use simulated annealing to solve for the optimal coseismic and aftershock slip distributions. We then use this optimal model and use simulated annealing to solve for the associated optimal frictional properties. Having determined reasonable values for all parameters, we proceed to the joint inversion, using a Bayesian inversion scheme to simultaneously solve for coseismic and aftershock slip as well as the frictional properties and InSAR offsets. We use a Monte Carlo Markov Chain method where the step size is adjusted if acceptance rates become too high or too low (Amey et al., 2018). However, the parameter step size is fixed once the burn-in has been passed, and samples are drawn from the posterior probability distribution.

4.2. Results

We performed a synthetic test to validate the new model and examine trade-offs between various parameters. A more detailed analysis of these results can be found in the supporting information (see Text S4 and Figures S17 and S18). The synthetic earthquake and associated afterslip can be well retrieved by the inversion and the frictional properties and depth dependence can be retrieved within error. Having tested the model and understood some of the trade-offs, we proceeded to use it on real data.

We use the best fixed geometries inferred in section 3.4, extended along strike and divided in to 10 km square patches. After the simulated annealing stages, the Bayesian inversion algorithm keeps a record of model samples. After completion of the inversion and removal of any burn-in, the kept models provide joint
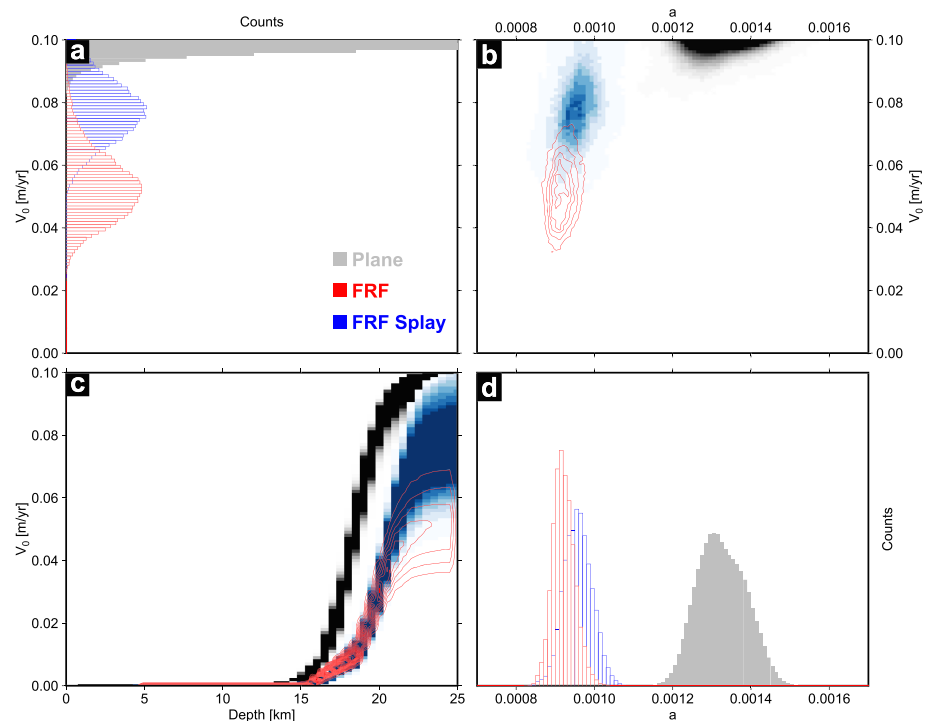
Figure 10. Comparison between the distributions of frictional properties for each geometry. (a) Probability density function (PDF) of V_0. (b) Joint PDFs for V_0 and a. (c) Variation of V_0 with depth. (d) PDF of a.

probability distributions for all model parameters. Results for the planar geometry are shown in Figures 7, 8, 9, and 10. Figure S19 shows an example of the temporal evolution of different slip patches in the planar model as well as the difference that including the InSAR data makes to the inversion.

All three geometries are capable of explaining the majority of coseismic, aftershock, and postseismic data with VR of over 99% for all three models. VR was calculated using all the data used in the modeling (i.e., InSAR and GNSS data from the InSAR acquisition times). Furthermore, examination of the spatial distribution of residuals does not clearly favor one geometry over any other (see Figure S20). Coseismic slip distributions for all three geometries are similar except where deeper slip in the planar and FRF models is mapped on to the shallow splay in the FRF splay model. Postseismic slip is primarily downdip of the coseismic rupture in all cases, with the majority of slip fringing the downdip edge of the main rupture. The FRF splay model has some possible shallow postseismic slip on the splay, probably caused by the low normal stresses on the fault at these depths. A similar mechanism may explain the shallow afterslip seen on the Main Dun thrust by Elliott et al. (2016).

Figure 10 shows a comparison between the values of a and V_0 inferred for each geometry. The results for the FRF and FRF splay models are very similar and within error of one another but distinct from the results for the planar geometry. This suggests that the inclusion of a ramp has a significant effect on the inferred frictional properties, requiring lower values for both a and V_0.

5. Discussion

5.1. Postseismic Deformation

Our assessment of the postseismic deformation following the Gorkha event largely agrees with previous work (Gualandi et al., 2016; Jiang et al., 2018; Mencin et al., 2016; Sreejith et al., 2016; Wang & Fialko, 2018; Zhao et al., 2017). GNSS and InSAR measurements show that postseismic deformation is relatively localized and predominantly north (downdip) of the coseismic deformation. Our measurements confirm there is very little motion to the south of the Gorkha coseismic slip region. Elliott et al. (2016) observed limited afterslip (<6 cm LOS) on the Main Dun Thrust using Sentinel-1 interferograms, which we confirm is also visible in ALOS interferograms. Bai et al. (2016) suggested the aftershocks with steep nodal planes may have occurred on splay faults above the main ramp, suggesting possible activity following the earthquake. Postseismic slip

on thrust faults may play a role in the development of topography (e.g., Nishimura et al., 2008; Copley, 2014; Copley & Reynolds, 2014) and may contribute to the maintenance of taper in a critical taper wedge.

Modeling of the deformation reveals that rate-strengthening afterslip can explain the majority of geodetic data (VR > 99% for data used in modeling), although some limited viscoelastic relaxation is possible. The inferred afterslip does not extend significantly along strike, with most deformation directly downdip of the coseismic rupture. This means the region to the west of the Gorkha event highlighted by Avouac et al. (2015) has not released significant seismic moment as afterslip. Mencin et al. (2016) argue that this limited afterslip points to strain reservoirs in the Himalaya which may contribute to large, surface-rupturing events along the MFT. Areas updip and along strike of the Gorkha event could still release their accumulated strain in future earthquakes.

5.2. Geometry of the Himalayan Fault System

We have presented the key constraints provided by seismic cycle geodesy in Nepal and discussed the variety of models which are permitted. As pointed out by Taylor (2016), different solutions can be obtained depending upon the philosophical approach used (see Figures 5 and 6). We have sought geometric models which are simultaneously capable of matching geodetic data from coseismic, postseismic, and interseismic data. Such an approach can be used more generally to determine the range of fault geometries permitted in different tectonic settings. However, our results show that such an approach will often need to be combined with other data sets to better constrain the full geometry and we discuss this further below.

Coseismic data requires there to be a shallowly dipping fault, extending from near the MFT surface trace to approximately 80 km north of the MFT. All of the proposed geometries, and our own inversions, agree on this aspect of the geometry (see Figures 5 and S7). Slip in the largest aftershock also agrees with this geometry. It does not seem necessary to include a shallow splay fault, as proposed by Whipple et al. (2016), to explain the "uplift anomaly" they identify in the coseismic deformation field. This anomaly is seen in profiles through the eastern section of the coseismic InSAR data as a secondary peak to the north of the primary coseismic uplift signal. This welt of uplift is seen more clearly in some InSAR tracks than others and is difficult to explain perfectly in all InSAR tracks with any of our models. All of the proposed models explain the uplift anomaly to a similar degree. Planar models do so by placing slip further north on the flat and FRF and FRF splay models do so by having some slip on the ramp and/or splay fault (compare coseismic slip in Figures S6, S8, and S10 in the supporting information).

Postseismic and interseismic deformation suggest there is a shallowly dipping plane extending northward with a depth of approximately 20 km between 120 and 140 km from the MFT. Geometries with deeper faults at these distances (e.g., Elliott et al., 2016; Hubbard et al., 2016) cannot reproduce the relatively short wavelength of the postseismic deformation field.

Any geometry for the Himalayan fault system therefore needs to contain two shallowly dipping fault segments at slightly different depths to explain both the coseismic and postseismic data. Unfortunately, our current suite of geodetic data cannot readily distinguish between the various proposals for how these two segments are connected. A single plane can explain the data reasonably well, but so can a geometry involving one or multiple ramps and splays.

In addition, our assumption that there is a single structure which accommodates strain throughout the earthquake cycle may be too simplistic. The apparent mismatch between the location of the midcrustal ramp inferred using coseismic data (Elliott et al., 2016) and that suggested by our modeling may hint at different structures active at different times (compare yellow and cyan lines for the FRF geometry in Figure 5). It may be that one ramp was active during the earthquake and a more northerly ramp was active following the earthquake. Such a combination of active ramps could be indicative of a duplexing process, as inferred by studies of interseismic deformation (Grandin et al., 2012; Lindsey et al., 2018).

To make further progress, the constraints provided by geodesy need to be combined with those provided by other data sets in order to distinguish between various proposed geometries. For example, while a single planar geometry can reproduce the geodetic data, it offers no explanation for the spatial variation in long-term uplift rates seen in the Himalaya (e.g., Hodges et al., 2004; Lavé & Avouac, 2001; Wobus et al., 2005). Therefore, geometries including a midcrustal ramp or out-of-sequence thrusting on splay faults are proposed as explanations, both of which also satisfy the geodetic data. Additional data sets can also be used, such as

surface geology (Hubbard et al., 2016), microseismicity (Pandey et al., 1995), or seismic imaging (Duputel et al., 2016), each of which provide different constraints on allowable geometries.

Multidisciplinary studies are therefore necessary if we are to fully constrain the geometry and tectonics of the faults beneath Nepal. The geological modeling approach used by Hubbard et al. (2016) may be one way of conducting such interdisciplinary studies. Their model satisfies the constraints provided by geology and is corroborated by the distribution of slip in the Gorkha earthquake (Grandin et al., 2015; Qiu et al., 2016), potential dip variations in the earthquake itself (Zhang et al., 2017) and the locations of aftershocks (Wang et al., 2017). However, corroboration is not necessarily equivalent to confirmation of such a model. Riesner et al. (2017) highlight the need to include various data sets and account for their relative uncertainties when constructing such geological models. In order to do this, future multidisciplinary studies should not only use multiple kinds of data but also contain the expertise necessary to account for the range of permissible models that can fit such data. This strategy should also be used more generally, where possible, to provide tighter constraints on fault geometries in a variety of tectonic contexts.

5.3. Frictional Properties

We developed a joint inversion algorithm that simultaneously solves for coseismic slip and fault frictional properties assuming rate-strengthening friction. We demonstrated that the inversion could successfully retrieve the frictional properties and coseismic slip distribution for a synthetic earthquake model. This method allows for the propagation of errors from the coseismic slip inversion in to errors in the inferred frictional properties. Our approach is generally applicable to fault systems undergoing frictional afterslip in response to coseismic stress transfer and could be adapted for use in other areas where we have both coseismic and postseismic deformation data.

Our model implementation depends on a number of simplifying assumptions such as perfect elasticity in a uniform half-space, minimal viscoelastic relaxation, lithostatic normal stresses, and a simplification of the rate-and-state friction laws. We applied our joint inversion to coseismic and postseismic data from Nepal, retrieving values for a in the range 0.8–1.6×10^{-3}, depending on the geometry of the fault system. These values are at the lower end of those retrieved from laboratory experiments, which are typically on the order of 10^{-3} to 10^{-2} (Marone, 1998; van den Ende et al., 2018). If we assume hydrostatic or effective pressure rather than lithostatic pressure, then our values of a increase accordingly.

Wang and Fialko (2018) used a similar rate-strengthening friction law to explain postseismic deformation and found values for V_0 and a of 10 m/yr and 6.5×10^{-2}, respectively. They used a locking width to force slip only downdip of the rupture and found that a locking width of 110 km provides the best fit, which is in reasonable agreement with our results. We also found that our values for a and V_0 were significantly smaller than those inferred by Wang and Fialko (2018). Wang and Fialko (2018) solve for $a\sigma$ rather than incorporating a lithostatic normal stress as we do. Using a depth of 15 km for the region of postseismic slip, lithostatic pressure is approximately 400 MPa which gives us a value for $a\sigma$ of 0.32–0.64 MPa, which is still an order of magnitude less than those obtained by Wang and Fialko (2018). This may be due to the slightly different geometries, different locking widths, different model setup or different input data. However, our results for the planar geometry are consistent with those found in other studies of postseismic deformation, where $a\sigma$ is on the order of 0.1–10 MPa and V_0 on the order of the interseismic loading rate (Barbot et al., 2009; Chang et al., 2013; Feng et al., 2016; Rollins et al., 2015; Wimpenny et al., 2017).

We found that all three geometries were capable of reproducing the majority of main shock, aftershock, and postseismic displacements using physically coupled coseismic and postseismic slip. VR for all three geometries was over 99% for the data used in the modeling, with only small differences between them. The addition of a shallow splay fault gives a slight increase in VR, as might be expected given the extra complexity of the model (81 more slip patches and an additional V_0 value). Overall though, we suggest that the minor differences in VR mean that the three geometries are equally capable of explaining the observations both kinematically and dynamically.

The inferred frictional properties depend on the geometry used, primarily on whether a midcrustal ramp is included in the model. A midcrustal ramp means patches downdip of the Gorkha rupture are deeper and thus have a higher lithostatic normal stress in our models. Furthermore, the more steeply dipping ramp affects the stress change experienced by all patches on and below the ramp as well as the impact that slip on
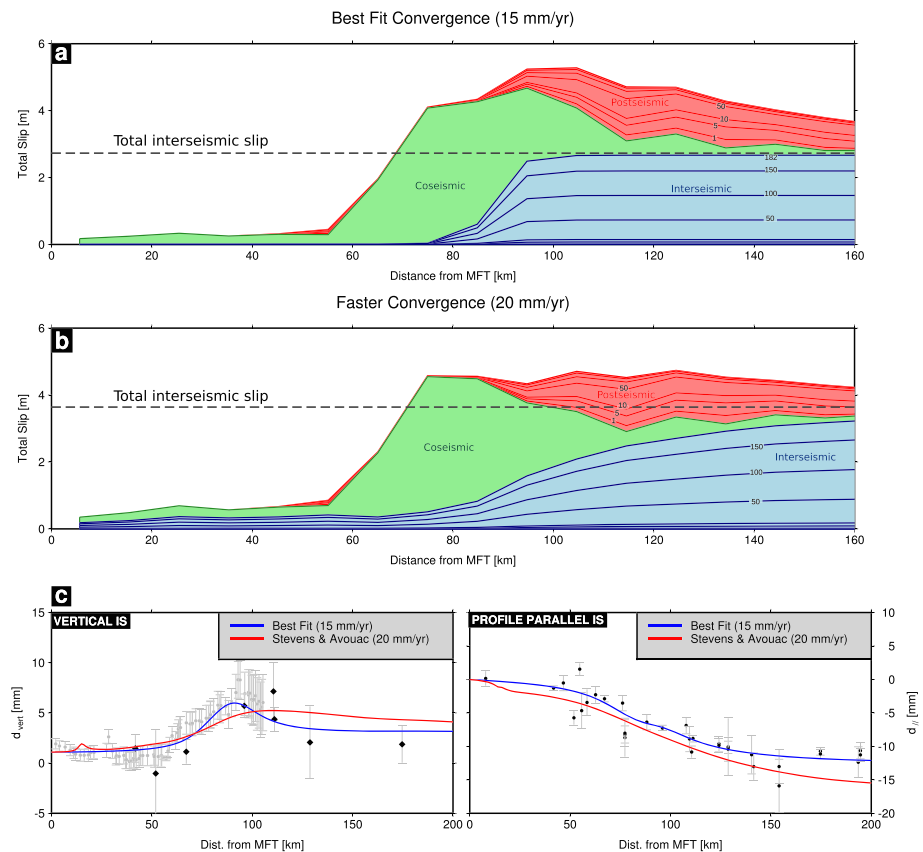
Figure 11. Slip budget for different scenarios in Nepal. (a) Total slip between the 1833 and 2015 earthquakes. Different colors refer to slip in different parts of the earthquake cycle. Small numbers along slip contours correspond to the number of years over which the slip has accrued. Dashed line is the total slip which needs to be released over the period. (b) Same as (a), except using a convergence rate of 20 mm/yr and interseismic slip derived from Stevens and Avouac (2015). (c) Fit of the different interseismic slip models to interseismic data prior to the 2015 Gorkha earthquake.

these patches has on the surface deformation field. This combination of factors means that a different set of frictional properties are required in order to match the surface deformation observations.

5.4. Long-Term Slip Budget

To test whether the long-term slip budget is balanced, we compared the results of our rate-strengthening afterslip model with the interseismic slip rates suggested by our kinematic modeling of profiles, and the interseismic rates suggested by Stevens and Avouac (2015). We used the results for the planar geometry and calculated the total seismic and aseismic slip for different scenarios. We used the mode coseismic slip and mean frictional properties for each patch on the planar geometry and then take the average of patches along strike to give downdip coseismic and postseismic slip distributions. First, we assumed that the 1833 earthquake released all the slip deficit in the region of the 2015 Gorkha event and that the two events were similar in nature (Mencin et al., 2016). The 1833 event had a similar magnitude to the 2015 event (M_w 7.5–7.9) and occurred near to Kathmandu, failing to rupture the surface (Bilham, 1995; Mugnier et al., 2013). We compared the accumulated interseismic slip between the 1833 earthquake with the coseismic and postseismic slip in the Gorkha event (Figure 11a). In this scenario, the coseismic and postseismic slips lead to a slip surplus for distances greater than approximately 70 km from the MFT. Such a situation seems unlikely and arises because our kinematic models suggest significant interseismic slip occurs over a similar range as both coseismic and postseismic slip (e.g., see Figure 5). This surplus could be partly resolved if interseismic slip rates vary through time: lower slip rates in the region of coseismic slip over part of the interseismic period would lead to less of a slip surplus.

Alternatively, the convergence rate may be higher than the 15 mm/yr suggested by our modeling of the interseismic data. We therefore increased the convergence rate to 20 mm/yr, as suggested by Stevens and

Avouac (2015), and used their coupling model to calculate interseismic velocities over the MFT. The average downdip velocities are then projected onto a profile to give the results in Figure 11b. Figure 11c shows the fit of this interseismic model to the profile data. The higher overall convergence rate, combined with a more gradual transition from locked to sliding on the fault is capable of matching the main features of the interseismic deformation, although not as well as the best fit kinematic model. The slip surplus in this model is smaller than our kinematic models. Given the assumptions and simplifications used in our calculations, this surplus may not be significantly different from no slip surplus downdip of the Gorkha rupture.

Nevertheless, in both models, there are parts of the fault which either show a slip surplus or a slip deficit. Stevens and Avouac (2015) have shown that the long-term slip rates, measured geologically along the Himalayan arc, closely resemble the short term convergence rates measured using geodesy. This suggests the seismic cycle should approximately balance, with almost all convergence being transferred to the frontal thrusts along the MFT. Small, local slip surpluses or deficits may be present in our models because our models do not cover a long enough time period or because of our geometric simplifications and averaging along strike. Alternatively, small slip surpluses may indicate permanent deformation which is not transferred all the way to the front, thereby proving a means of growing topography (Meade, 2010).

Whatever assumptions are used for our models, a significant slip deficit exists updip of the Gorkha coseismic rupture. If the 1833 earthquake ruptured to the front and released any accumulated strain there, then the total updip slip deficit is equal to the convergence rate multiplied by the total time. Convergence rates of 15–20 mm/yr give slip deficits of 2.7–3.7 m updip of the Gorkha rupture. On the other hand, if the 1833 event did not rupture to the front, but was instead similar to the Gorkha event, then the last time slip was released to the front may have been 1505. Using the same convergence rates as above gives slip deficits of 7.7–10.3 m. Mencin et al. (2016) have highlighted the role that Gorkha type events may play in transferring strain to the frontal portion of the Himalayan fold and thrust belt, accruing a large strain reservoir which could rupture in future events. We can estimate an approximate magnitude range for possible future earthquakes which rupture the whole region updip of the Gorkha event (rupture length of 110 km and downdip width of 70 km). We obtain moment magnitudes (M_w) in the range 7.8–8.3 for the different slip deficits discussed above. However, larger events would be possible, either due to the slip deficit being higher or due to this updip region slipping as part of an earthquake nucleating deeper in the fault system, in a similar location to the Gorkha event.

6. Conclusions

We processed InSAR and GNSS data to obtain measurements of near-field postseismic deformation following the M_w7.8 Gorkha earthquake in Nepal. We obtained a similar deformation field to previous studies (Gualandi et al., 2016; Jiang et al., 2018; Mencin et al., 2016; Sreejith et al., 2016; Wang & Fialko, 2018; Zhao et al., 2017), which is predominantly produced by afterslip. Furthermore, this afterslip does not reduce any of the slip deficit updip of the coseismic rupture, and this deficit may be many meters and capable of producing earthquakes with moment magnitudes in the range 7.8–8.3.

We then combined these data with coseismic and interseismic geodetic data to investigate the geometry of the Himalayan fault system. We found that the data required a shallowly dipping fault until at least 80 km north of the MFT surface trace. Our combined data could not conclusively distinguish between different possible geometries north of this point.

We developed a joint inversion which seeks models which simultaneously fit the coseismic, aftershock, and postseismic deformation fields. The inversion uses a rate-strengthening friction law to link the coseismic and postseismic slip by solving for the frictional properties (a and V_0). We found that afterslip, caused by stress changes associated with the main shock and aftershock, could explain most of the postseismic data. We found a to be between 0.8–1.6×10^{-3}, in agreement with laboratory experiments and postseismic deformation studies of other earthquakes. This range of a values could be used in future simulations of the earthquake cycle in the Nepal Himalaya to better understand potential hazards in the region.

All three proposed geometries are capable of explaining over 99% of the data variance and thus fail to provide an alternative way of distinguishing the most appropriate model. It therefore seems necessary to increase the quantity, quality, and diversity of data in the Nepal Himalaya. Furthermore, these data need to be correctly

integrated by multidisciplinary teams with the expertise to understand the errors and limitations of each data set. New models are also required to adequately model each of the data sets and tie them together.

References

Ader, T., Avouac, J.-P., Liu-Zeng, J., Lyon-Caen, H., Bollinger, L., Galetzka, J., et al. (2012). Convergence rate across the Nepal Himalaya and interseismic coupling on the Main Himalayan Thrust: Implications for seismic hazard. *Journal of Geophysical Research*, *117*, B04403. https://doi.org/10.1029/2011JB009071

Adhikari, L., Gautam, U., Koirala, B., Bhattarai, M., Kandel, T., Gupta, R., et al. (2015). The aftershock sequence of the 2015 April 25 Gorkha Nepal earthquake. *Geophysical Journal International*, *203*(3), 2119–2124. https://doi.org/10.1093/gji/ggv412

Amey, R. M. J., Hooper, A., & Walters, R. J. (2018). A Bayesian method for incorporating self-similarity into earthquake slip inversions. *Journal of Geophysical Research: Solid Earth*, *123*, 6052–6071. https://doi.org/10.1029/2017JB015316

Avouac, J.-P., Meng, L., Wei, S., Wang, T., & Ampuero, J.-P. (2015). Lower edge of locked Main Himalayan Thrust unzipped by the 2015 Gorkha earthquake. *Nature Geoscience*, *8*(9), 708–711. https://doi.org/10.1038/ngeo2518

Bagnardi, M., & Hooper, A. J. (2017). GBIS (Geodetic Bayesian Inversion Software): Rapid inversion of InSAR and GNSS data to estimate surface deformation source parameters and uncertainties. In *American Geophysical Union, Fall Meeting 2017, abstract #G23A-0881*.

Bai, L., Liu, H., Ritsema, J., Mori, J., Zhang, T., Ishikawa, Y., & Li, G. (2016). Faulting structure above the Main Himalayan Thrust as shown by relocated aftershocks of the 2015 M_w 7.8 Gorkha, Nepal, earthquake. *Geophysical Research Letters*, *43*, 637–642. https://doi.org/10.1002/2015GL066473

Barbot, S., & Fialko, Y. (2010). A unified continuum representation of post-seismic relaxation mechanisms: Semi-analytic models of afterslip, poroelastic rebound and viscoelastic flow. *Geophysical Journal International*, *182*(3), 1124–1140. https://doi.org/10.1111/j.1365-246X.2010.04678.x

Barbot, S., Fialko, Y., & Bock, Y. (2009). Postseismic deformation due to the M_w 6.0 2004 Parkfield earthquake: Stress-driven creep on a fault with spatially variable rate-and-state friction parameters. *Journal of Geophysical Research*, *114*, B07405. https://doi.org/10.1029/2008JB005748

Bekaert, D. P. S., Hooper, A., & Wright, T. J. (2015). *A spatially-variable power-law tropospheric correction technique for InSAR data* (Vol. 120, pp. 1345–1356). https://doi.org/10.1002/2014JB011558

Bekaert, D., Walters, R., Wright, T., Hooper, A., & Parker, D. (2015). Statistical comparison of inSAR tropospheric correction techniques. *Remote Sensing of Environment*, *170*, 40–47. https://doi.org/10.1016/j.rse.2015.08.035

Ben Thompson, T., & Meade, B. J. (2018). Topography and the shallow slip deficit inference. https://doi.org/10.31223/OSF.IO/PUZ84

Bettinelli, P., Avouac, J.-P., Flouzat, M., Jouanne, F., Bollinger, L., Willis, P., & Chitrakar, G. R. (2006). Plate motion of India and interseismic strain in the Nepal Himalaya from GPS and DORIS measurements. *Journal of Geodesy*, *80*(8-11), 567–589. https://doi.org/10.1007/s00190-006-0030-3

Bilham, R. (1995). *Location and magnitude of the 1833 Nepal earthquake and its relation to the rupture zones of contiguous great Himalayan earthquakes*. https://doi.org/10.2307/24097233

Bilham, R., & Wallace, K. (2005). Future $M_w > 8$ earthquakes in the Himalaya: Implications from the 26 Dec 2004 $M_w = 9.0$ earthquake on India's eastern plate margin. *Geological Survey of India Special Publication*, *85*(85), 1–14.

Bonini, L., Toscani, G., & Seno, S. (2014). Three-dimensional segmentation and different rupture behavior during the 2012 Emilia seismic sequence (northern Italy). *Tectonophysics*, *630*, 33–42. https://doi.org/10.1016/j.tecto.2014.05.006

Chang, S.-H., Avouac, J.-P., Barbot, S., & Lee, J.-C. (2013). Spatially variable fault friction derived from dynamic modeling of aseismic afterslip due to the 2004 Parkfield earthquake. *Journal of Geophysical Research: Solid Earth*, *118*, 3431–3447. https://doi.org/10.1002/jgrb.50231

Copley, A. (2014). Postseismic afterslip 30 years after the 1978 Tabas-e-Golshan (Iran) earthquake: Observations and implications for the geological evolution of thrust belts. *Geophysical Journal International*, *197*(2), 665–679. https://doi.org/10.1093/gji/ggu023

Copley, A., & Jolivet, R. (2016). Fault rheology in an aseismic fold-thrust belt (Shahdad, eastern Iran). *Journal of Geophysical Research: Solid Earth*, *121*, 412–431. https://doi.org/10.1002/2015JB012431

Copley, A., & Reynolds, K. (2014). Imaging topographic growth by long-lived postseismic afterslip at Sefidabeh, east Iran. *Tectonics*, *33*(3), 330–345. https://doi.org/10.1002/2013TC003462

Decriem, J., Árnadóttir, T., Hooper, A., Geirsson, H., Sigmundsson, F., Keiding, M., et al. (2010). The 2008 May 29 earthquake doublet in SW Iceland. *Geophysical Journal International*, *181*, 1128–1146. https://doi.org/10.1111/j.1365-246X.2010.04565.x

Duputel, Z., Agram, P. S., Simons, M., Minson, S. E., & Beck, J. L. (2014). Accounting for prediction uncertainty when inferring subsurface fault slip. *Geophysical Journal International*, *197*(1), 464–482. https://doi.org/10.1093/gji/ggt517

Duputel, Z., Vergne, J., Rivera, L., Wittlinger, G., Farra, V., & Hetényi, G. (2016). The 2015 Gorkha earthquake: A large event illuminating the Main Himalayan Thrust fault. *Geophysical Research Letters*, *43*, 2517–2525. https://doi.org/10.1002/2016GL068083

Elliott, J. R., Biggs, J., Parsons, B., & Wright, T. J. (2008). InSAR slip rate determination on the Altyn Tagh fault, northern Tibet, in the presence of topographically correlated atmospheric delays. *Geophysical Research Letters*, *35*, L12309. https://doi.org/10.1029/2008GL033659

Elliott, J., Jolivet, R., González, P. J., Avouac, J.-P., Hollingsworth, J., Searle, M. P., & Stevens, V. (2016). Himalayan megathrust geometry and relation to topography revealed by the Gorkha earthquake. *Nature Geoscience*, *9*(2), 174–180. https://doi.org/10.1038/ngeo2623

Elliott, J. R., Parsons, B., Jackson, J. A., Shan, X., Sloan, R. A., & Walker, R. T. (2011). Depth segmentation of the seismogenic continental crust: The 2008 and 2009 Qaidam earthquakes. *Geophysical Research Letters*, *38*, L06305. https://doi.org/10.1029/2011GL046897

Feng, L., Barbot, S., Hill, E. M., Hermawan, I., Banerjee, P., & Natawidjaja, D. H. (2016). Footprints of past earthquakes revealed in the afterslip of the 2010 M_w 7.8 Mentawai tsunami earthquake. *Geophysical Research Letters*, *43*, 9518–9526. https://doi.org/10.1002/2016GL069870

Freed, A. M. (2007). Afterslip (and only afterslip) following the 2004 Parkfield, California, earthquake. *Geophysical Research Letters*, *34*, L06312. https://doi.org/10.1029/2006GL029155

Freed, A. M., Bürgmann, R., & Herring, T. (2007). Far-reaching transient motions after Mojave earthquakes require broad mantle flow beneath a strong crust. *Geophysical Research Letters*, *34*, L19302. https://doi.org/10.1029/2007GL030959

Fukuda, J., & Johnson, K. M. (2008). A fully Bayesian inversion for spatial distribution of fault slip with objective smoothing. *Bulletin of the Seismological Society of America*, *98*(3), 1128–1146. https://doi.org/10.1785/0120070194

Galetzka, J., Melgar, D., Genrich, J. F., Geng, J., Owen, S., Lindsey, E. O., et al. (2015). Slip pulse and resonance of the Kathmandu basin during the 2015 Gorkha earthquake, Nepal. *Science*, *349*(6252), 1091–1095.

Grandin, R., Doin, M.-P., Bollinger, L., Pinel-Puyssegur, B., Ducret, G., Jolivet, R., & Sapkota, S. N. (2012). Long-term growth of the Himalaya inferred from interseismic inSAR measurement. *Geology*, *40*(12), 1059–1062. https://doi.org/10.1130/G33154.1

Grandin, R., Vallée, M., Satriano, C., Lacassin, R., Klinger, Y., Simoes, M., & Bollinger, L. (2015). Rupture process of the $M_w = 7.9$ 2015 Gorkha earthquake (Nepal): Insights into Himalayan megathrust segmentation. *Geophysical Research Letters*, *42*, 8373–8382. https://doi.org/10.1002/2015GL066044

Gualandi, A., Avouac, J.-P., Galetzka, J., Genrich, J. F., Blewitt, G., Bijaya Adhikari, L., et al. (2016). Pre-and post-seismic deformation related to the 2015 M_w 7.8 Gorkha earthquake, Nepal. *Tectonophysics*, *714–715*, 90–106. https://doi.org/10.1016/j.tecto.2016.06.014

Hao, M., Shen, Z.-K., Wang, Q., & Cui, D. (2012). Postseismic deformation mechanisms of the 1990 M_w 6.4 Gonghe, China earthquake constrained using leveling measurements. *Tectonophysics*, *532-535*, 205–214. https://doi.org/10.1016/j.tecto.2012.02.005

Hearn, E. H. (2002). Dynamics of Izmit earthquake postseismic deformation and loading of the Duzce earthquake hypocenter. *Bulletin of the Seismological Society of America*, *92*(1), 172–193. https://doi.org/10.1785/0120000832

Herring, T. A., King, R. W., & McClusky, S. C. (2013). Introduction to GAMITGLOBK Release 10.5.

Hodges, K. V., Wobus, C., Ruhl, K., Schildgen, T., & Whipple, K. (2004). Quaternary deformation, river steepening, and heavy precipitation at the front of the higher Himalayan ranges. *Earth and Planetary Science Letters*, *220*(3-4), 379–389. https://doi.org/10.1016/S0012-821X(04)00063-9

Hooper, A., Bekaert, D., Spaans, K., & ArÄ, M. (2012). Recent advances in SAR interferometry time series analysis for measuring crustal deformation. *Tectonophysics*, *514-517*, 1–13. https://doi.org/10.1016/j.tecto.2011.10.013

Huang, M.-H., Tung, H., Fielding, E. J., Huang, H.-H., Liang, C., Huang, C., & Hu, J.-C. (2016). Multiple fault slip triggered above the 2016 M_w 6.4 Meinong earthquake in Taiwan. *Geophysical Research Letters*, *43*, 7459–7467. https://doi.org/10.1002/2016GL069351

Hubbard, J., Almeida, R., Foster, A., Sapkota, S. N., Bürgi, P., & Tapponnier, P. (2016). Structural segmentation controlled the 2015 M_w 7.8 Gorkha earthquake rupture in Nepal. *Geology*, *44*(8), 639–642. https://doi.org/10.1130/G38077.1

Hubbard, J., Barbot, S., Hill, E. M., & Tapponnier, P. (2015). Coseismic slip on shallow décollement megathrusts: Implications for seismic and tsunami hazard. *Earth-Science Reviews*, *141*, 45–55. https://doi.org/10.1016/J.EARSCIREV.2014.11.003

Hussain, E., Wright, T. J., Walters, R. J., Bekaert, D., Hooper, A., & Houseman, G. A. (2016). Geodetic observations of postseismic creep in the decade after the 1999 Izmit earthquake, Turkey: Implications for a shallow slip deficit. *Journal of Geophysical Research: Solid Earth*, *121*, 2980–3001. https://doi.org/10.1002/2015JB012737

Ingleby, T., & Wright, T. J. (2017). Omori-like decay of postseismic velocities following continental earthquakes. *Geophysical Research Letters*, *44*, 3119–3130. https://doi.org/10.1002/2017GL072865

Jackson, M., & Bilham, R. (1994). Constraints on Himalayan deformation inferred from vertical velocity fields in Nepal and Tibet. *Journal of Geophysical Research*, *99*(B7), 13,897–13,912. https://doi.org/10.1029/94JB00714

Jiang, Z., Yuan, L., Huang, D., Yang, Z., & Hassan, A. (2018). Postseismic deformation associated with the 2015 M_w 7.8 Gorkha earthquake, Nepal: Investigating ongoing afterslip and constraining crustal rheology. *Journal of Asian Earth Sciences*, *156*, 1–10. https://doi.org/10.1016/J.JSEAES.2017.12.039

Jolivet, R., Grandin, R., Lasserre, C., Doin, M.-P., & Peltzer, G. (2011). Systematic inSAR tropospheric phase delay corrections from global meteorological reanalysis data. *Geophysical Research Letters*, *38*, L17311. https://doi.org/10.1029/2011GL048757

Jolivet, R., Simons, M., Agram, P. S., Duputel, Z., & Shen, Z.-K. (2015). Aseismic slip and seismogenic coupling along the central San Andreas Fault. *Geophysical Research Letters*, *42*, 297–306. https://doi.org/10.1002/2014GL062222

Jónsson, S., Segall, P., Pedersen, R., & Björnsson, G. (2003). Post-earthquake ground movements correlated to pore-pressure transients. *Nature*, *424*(6945), 179–183. https://doi.org/10.1038/nature01776

Kreemer, C., Blewitt, G., & Klein, E. C. (2014). A geodetic plate motion and global strain rate model. *Geochemistry, Geophysics, Geosystems*, *15*, 3849–3889. https://doi.org/10.1002/2014GC005407

Lavé, J., & Avouac, J. P. (2001). Fluvial incision and tectonic uplift across the Himalayas of central Nepal. *Journal of Geophysical Research*, *106*(B11), 26,561–26,591. https://doi.org/10.1029/2001JB000359

Lindsey, E. O., Almeida, R., Mallick, R., Hubbard, J., Bradley, K., Tsang, L. L. H., et al. (2018). Structural control on downdip locking extent of the Himalayan megathrust. *Journal of Geophysical Research: Solid Earth*, *123*, 5265–5278. https://doi.org/10.1029/2018JB015868

Lindsey, E. O., Natsuaki, R., Xu, X., Shimada, M., Hashimoto, M., Melgar, D., & Sandwell, D. T. (2015). Line-of-sight displacement from ALOS-2 interferometry: M_w 7.8 Gorkha earthquake and M_w 7.3 aftershock. *Geophysical Research Letters*, *42*, 6655–6661. https://doi.org/10.1002/2015GL065385

Lohman, R. B., & Simons, M. (2005). Some thoughts on the use of inSAR data to constrain models of surface deformation: Noise structure and data downsampling. *Geochemistry, Geophysics, Geosystems*, *6*, Q01007. https://doi.org/10.1029/2004GC000841

Marone, C. (1998). Laboratory-derived friction laws and their application to seismic faulting. *Annual Review of Earth and Planetary Sciences*, *26*, 643–696.

Meade, B. J. (2010). The signature of an unbalanced earthquake cycle in Himalayan topography? *Geology*, *38*(11), 987–990. https://doi.org/10.1130/G31439.1

Mencin, D., Bendick, R., Upreti, B. N., Adhikari, D. P., Gajurel, A., Bhattarai, R. R., et al. (2016). Himalayan strain reservoir inferred from limited afterslip following the Gorkha earthquake. *Nature Geoscience*, *9*(7), 533–537. https://doi.org/10.1038/ngeo2734

Mosegaard, K., & Tarantola, A. (1995). Monte Carlo sampling of solutions to inverse problems. *Journal of Geophysical Research*, *100*(B7), 12,431–12,447. https://doi.org/10.1029/94JB03097

Mugnier, J.-L., Gajurel, A., Huyghe, P., Jayangondaperumal, R., Jouanne, F., & Upreti, B. (2013). Structural interpretation of the great earthquakes of the last millennium in the central Himalaya. *Earth-Science Reviews*, *127*, 30–47. https://doi.org/10.1016/J.EARSCIREV.2013.09.003

Nishimura, T., Tobita, M., Yarai, H., Amagai, T., Fujiwara, M., Une, H., & Koarai, M. (2008). Episodic growth of fault-related fold in northern Japan observed by SAR interferometry. *Geophysical Research Letters*, *35*, L13301. https://doi.org/10.1029/2008GL034337

Okada, Y. (1985). Surface deformation due to shear and tensile faults in a half-space. *Bulletin of the Seismological Society of America*, *75*(4), 1135–1154.

Okada, Y. (1992). Internal deformation due to shear and tensile faults in a half-space. *Bulletin of the Seismological Society of America*, *82*(2), 1018–1040.

Oliver, M., & Webster, R. (2014). A tutorial guide to geostatistics: Computing and modelling variograms and kriging. *Catena*, *113*, 56–69. https://doi.org/10.1016/j.catena.2013.09.006

Pandey, M. R., Tandukar, R. P., Avouac, J. P., Lavé, J., & Massot, J. P. (1995). Interseismic strain accumulation on the Himalayan crustal ramp (Nepal). *Geophysical Research Letters*, *22*(7), 751–754. https://doi.org/10.1029/94GL02971

Perfettini, H., & Avouac, J.-P. (2004). Postseismic relaxation driven by brittle creep: A possible mechanism to reconcile geodetic measurements and the decay rate of aftershocks, application to the Chi-Chi earthquake, Taiwan. *Journal of Geophysical Research*, *109*, B02304. https://doi.org/10.1029/2003JB002488

Perfettini, H., Avouac, J.-P., Tavera, H., Kositsky, A., Nocquet, J.-M., Bondoux, F., et al. (2010). Seismic and aseismic slip on the central Peru megathrust. *Nature*, *465*(7294), 78–81. https://doi.org/10.1038/nature09062

Pollitz, F. F. (1997). Gravitational viscoelastic postseismic relaxation on a layered spherical Earth. *Journal of Geophysical Research*, *102*(B8), 17,921–17,941. https://doi.org/10.1029/97JB01277

Qiu, Q., Hill, E. M., Barbot, S., Hubbard, J., Feng, W., Lindsey, E. O., et al. (2016). The mechanism of partial rupture of a locked megathrust: The role of fault morphology. *Geology*, *44*(10), 875–878. https://doi.org/10.1130/G38178.1

Ragon, T., Sladen, A., & Simons, M. (2018). Accounting for uncertain fault geometry in earthquake source inversions I: Theory and simplified application. *Geophysical Journal International*, *214*(2), 1174–1190. https://doi.org/10.1093/gji/ggy187

Riesner, M., DurandRiard, P., Hubbard, J., Plesch, A., & Shaw, J. H. (2017). Building objective 3D fault representations in active tectonic settings. *Seismological Research Letters*, *88*(3), 831–839. https://doi.org/10.1785/0220160192

Rollins, C., Barbot, S., & Avouac, J.-P. (2015). Postseismic deformation following the 2010 $M = 7.2$ El Mayor-Cucapah earthquake: Observations, kinematic inversions, and dynamic models. *Pure and Applied Geophysics*, *172*, 1305–1358. https://doi.org/10.1007/s00024-014-1005-6

Rousset, B., Barbot, S., Avouac, J.-P., & Hsu, Y.-J. (2012). Postseismic deformation following the 1999 Chi-Chi earthquake, Taiwan: Implication for lower-crust rheology. *Journal of Geophysical Research*, *117*, B12405. https://doi.org/10.1029/2012JB009571

Ryder, I., Parsons, B., Wright, T. J., & Funning, G. J. (2007). Post-seismic motion following the 1997 Manyi (Tibet) earthquake: InSAR observations and modelling. *Geophysical Journal International*, *169*, 1009–1027. https://doi.org/10.1111/j.1365-246X.2006.03312.x

Sapkota, S. N., Bollinger, L., Klinger, Y., Tapponnier, P., Gaudemer, Y., & Tiwari, D. (2013). Primary surface ruptures of the great Himalayan earthquakes in 1934 and 1255. *Nature Geoscience*, *6*, 71–76.

Savage, J. C. (1990). Equivalent strike-slip earthquake cycles in half-space and lithosphere-asthenosphere Earth models. *Journal of Geophysical Research*, *95*(B4), 4873. https://doi.org/10.1029/JB095iB04p04873

Scholz, C. H. (1988). The critical slip distance for seismic faulting. *Nature*, *336*(6201), 761–763. https://doi.org/10.1038/336761a0

Sreejith, K. M., Sunil, P. S., Agrawal, R., Saji, A. P., Ramesh, D. S., & Rajawat, A. S. (2016). Coseismic and early postseismic deformation due to the 25 April 2015, M_w 7.8 Gorkha, Nepal, earthquake from InSAR and GPS measurements. *Geophysical Research Letters*, *43*, 3160–3168. https://doi.org/10.1002/2016GL067907

Stevens, V. L., & Avouac, J. P. (2015). Interseismic coupling on the Main Himalayan Thrust. *Geophysical Research Letters*, *42*, 5828–5837. https://doi.org/10.1002/2015GL064845

Taylor, M. H. (2016). Tales of Himalayan topography. *Nature Geoscience*, *9*(9), 649–651. https://doi.org/10.1038/ngeo2805

Taylor, M., & Yin, A. (2009). Active structures of the Himalayan-Tibetan orogen and their relationships to earthquake distribution, contemporary strain field, and Cenozoic volcanism. *Geosphere*, *5*(3), 199–214. https://doi.org/10.1130/GES00217.1

Thomas, M. Y., Avouac, J.-P., & Lapusta, N. (2017). Rate-and-state friction properties of the longitudinal valley fault from kinematic and dynamic modeling of seismic and aseismic slip. *Journal of Geophysical Research: Solid Earth*, *122*, 3115–3137. https://doi.org/10.1002/2016JB013615

van den Ende, M., Chen, J., Ampuero, J.-P., & Niemeijer, A. (2018). A comparison between rate-and-state friction and microphysical models, based on numerical simulations of fault slip. *Tectonophysics*, *733*, 273–295. https://doi.org/10.1016/J.TECTO.2017.11.040

Vergne, J., Cattin, R., & Avouac, J. P. (2001). On the use of dislocations to model interseismic strain and stress build-up at intracontinental thrust faults. *Geophysical Journal International*, *147*(1), 155–162. https://doi.org/10.1046/j.1365-246X.2001.00524.x

Wang, K., & Fialko, Y. (2015). Slip model of the 2015 M_w 7.8 Gorkha (Nepal) earthquake from inversions of ALOS-2 and GPS data. *Geophysical Research Letters*, *42*, 7452–7458. https://doi.org/10.1002/2015GL065201

Wang, K., & Fialko, Y. (2018). Observations and modeling of coseismic and postseismic deformation due to the 2015 M_w 7.8 Gorkha (Nepal) earthquake. *Journal of Geophysical Research: Solid Earth*, *123*, 761–779. https://doi.org/10.1002/2017JB014620

Wang, L., Hainzl, S., Zöller, G., & Holschneider, M. (2012). Stress- and aftershock-constrained joint inversions for coseismic and postseismic slip applied to the 2004 M6.0 Parkfield earthquake. *Journal of Geophysical Research*, *117*, B07406. https://doi.org/10.1029/2011JB009017

Wang, X., Wei, S., & Wu, W. (2017). Double-ramp on the Main Himalayan Thrust revealed by broadband waveform modeling of the 2015 Gorkha earthquake sequence. *Earth and Planetary Science Letters*, *473*, 83–93. https://doi.org/10.1016/j.epsl.2017.05.032

Wessel, P., & Smith, W. H. F. (1991). Free software helps map and display data, EOS. *Transactions American Geophysical Union*, *72*(41), 441–441. https://doi.org/10.1029/90EO00319

Whipple, K. X., Shirzaei, M., Hodges, K. V., & Arrowsmith, J. R. (2016). Active shortening within the Himalayan orogenic wedge implied by the 2015 Gorkha earthquake. *Nature Geoscience*, *9*, 711–716.

Wimpenny, S., Copley, A., & Ingleby, T. (2017). Fault mechanics and post-seismic deformation at Bam, SE Iran. *Geophysical Journal International*, *209*(2), 1018–1035. https://doi.org/10.1093/gji/ggx065

Wobus, C., Heimsath, A., Whipple, K., & Hodges, K. (2005). Active out-of-sequence thrust faulting in the central Nepalese Himalaya. *Nature*, *434*(7036), 1008–1011. https://doi.org/10.1038/nature03499

Wright, T. J., Elliott, J. R., Wang, H., & Ryder, I. (2013). Earthquake cycle deformation and the Moho: Implications for the rheology of continental lithosphere. *Tectonophysics*, *609*, 504–523.

Wright, T. J., Gonzalez, P. J., Walters, R. J., Hatton, E. L., Spaans, K., & Hooper, A. J. (2016). LiCSAR: Tools for automated generation of Sentinel-1 frame interferograms. American Geophysical Union, Fall General Assembly 2016, abstract #G23A-1037.

Zhang, Y., Wang, R., Walter, T. R., Feng, W., Chen, Y., & Huang, Q. (2017). Significant lateral dip changes may have limited the scale of the 2015 M_w 7.8 Gorkha earthquake. *Geophysical Research Letters*, *44*, 8847–8856. https://doi.org/10.1002/2017GL074095

Zhao, B., Bürgmann, R., Wang, D., Tan, K., Du, R., & Zhang, R. (2017). Dominant controls of downdip afterslip and viscous relaxation on the postseismic displacements following the M_w 7.9 Gorkha, Nepal, earthquake. *Journal of Geophysical Research: Solid Earth*, *122*, 8376–8401. https://doi.org/10.1002/2017JB014366